uOttawa

L'Université canadienne
Canada's university

FACULTÉ DES ÉTUDES SUPÉRIEURES ET POSTOCTORALES

uOttawa

L'Université canadienne
Canada's university

FACULTY OF GRADUATE AND POSDOCTORAL STUDIES

Robin Buckley
AUTEUR DE LA THÈSE / AUTHOR OF THESIS

M.A.Sc. (Electrical Engineering)
GRADE / DEGREE

School of Information Technology and Engineering
FACULTÉ, ÉCOLE, DÉPARTEMENT / FACULTY, SCHOOL, DEPARTMENT

Figures of Merit and Modelling of Metallo-Dielectric Waveguides

TITRE DE LA THÈSE / TITLE OF THESIS

P. Berini
DIRECTEUR (DIRECTRICE) DE LA THÈSE / THESIS SUPERVISOR

CO-DIRECTEUR (CO-DIRECTRICE) DE LA THÈSE / THESIS CO-SUPERVISOR

EXAMINATEURS (EXAMINATRICES) DE LA THÈSE / THESIS EXAMINERS

D. McNamara

J. Albert

Gary W. Slater
Le Doyen de la Faculté des études supérieures et postdoctorales / Dean of the Faculty of Graduate and Postdoctoral Studies

Figures of Merit and Modelling of Metallo-Dielectric Waveguides

by

Robin Buckley

A Thesis submitted to the Faculty of Graduate Studies and Postdoctoral Studies in partial fulfillment of the requirements for the degree of Master of Applied Science, Electrical Engineering

September 2008

Ottawa-Carleton Institute for Electrical and Computer Engineering
School of Information Technology and Engineering
University of Ottawa
Ottawa, Ontario, Canada

Your file Votre référence
ISBN: 978-0-494-46467-0
Our file Notre référence
ISBN: 978-0-494-46467-0

Abstract

The thesis is divided into two topics. The first is a figure of merit study on 2D surface plasmon waveguides, assessing the trade-off between attenuation and confinement. Three figures of merit are used since there are three separate, but equally effective, ways of measuring confinement. Different stripe geometries are considered in this analysis as well as a comparison between Au, Ag and Al (as the stripe metal) over the wavelength range from 200 to 2000 nm. The figures of merit are generally applicable and should be useful to help compare, assess and optimize designs in other 2D absorbing waveguides.

The second topic introduces a new waveguide structure, the metallo-dielectric waveguide, capable of aggressive bends and long-range propagation at optical wavelengths. Its design was inspired by the non-radiative dielectric waveguide which is effective at microwave frequencies but has been shown to have high loss at optical wavelengths. Since both waveguides use parallel plates as confinement mechanisms, one dimensional analysis is first performed to gain insight into their operation followed by full-wave 2D simulations of the two waveguides in their straight and curved form. Analysis of the parallel plates revealed the relation between the modes supported by the real metal and perfect electric conductors (PECs). The non-radiative dielectric waveguide is found to effectively suppress radiation; however, its propagation loss is high and the mode becomes deformed along radial bends, as $r_0 \rightarrow 0$, due to excitation of surface plasmon-polaritons. The newly introduced metallo-dielectric waveguide performs significantly better in that it is capable of long-range propagation while also supporting its fundamental TE mode along aggressive radial bends. This waveguide also has potential use in optoelectronic/electro-optic components due to the presence of the metal plates which could be used to apply electric fields or inject currents.

Acknowledgments

I dedicate this work to my mom who passed away from cancer during my undergrad degree. Despite what she was going through she always managed to keep a positive attitude while at the same time encouraging and supporting me in my studies.

I would like to thank Dr. Derek McNamara for projecting his enthusiasm and interest in electromagnetics onto me (and others) which encouraged me to pursue research in this area.

I would also like to thank my supervisor Dr. Pierre Berini for having introduced me to the field of plasmonics; I am indebted for the countless discussions along with the guidance he provided throughout my masters.

To my family, particularly Ed St.Cyr, and friends I thank you for being there for me in the best and worst of times. You guys mean more to me than you could ever imagine.

Contents

1 Introduction **7**

1.1 Background 7

1.2 Single-interface SPP 8

1.3 Thin film 11

1.4 Thesis outline 13

1.5 References 14

2 Figures of merit for 2D surface plasmon waveguides and application to metal stripes **15**

3 Long-Range Substantially Non-Radiative Metallo-Dielectric Waveguide **25**

4 Radiation Suppressing Metallo-Dielectric Optical Waveguides **33**

5 Conclusion **51**

5.1 Thesis contributions 51

5.2 Suggestions for future work 52

A On the convergence and accuracy of mode computations of surface plasmon waveguides **53**

Chapter 1

Introduction

1.1 Background

Transverse magnetic (TM) surface modes are known to exist at an interface between two materials which have a real part of permittivity of opposite sign. The optical properties of metals have been studied and shown through experimentation to exhibit a negative real part of permittivity at optical frequencies [1]. This property allows the metal-dielectric interface to support a Surface Plasmon-Polariton (SPP) mode at optical wavelengths which is bound through the coupling of electromagnetic waves to oscillations in conduction electrons at the surface of the metal [2].

The intensity of the SPP peaks at the interface then exponentially decay perpendicular to it [3]. This intensity (field) localization makes the waveguide ideal for sensing applications since small changes in the environment could have a large effect on the propagation of the SPP. Recent advances in nano-fabrication has sparked a widespread interest in this field. A number of well written reviews on the subject have been published by Barnes [4, 5], Maier [6] and Welford [7], for example.

This thesis will focus solely on the waveguiding properties of SPPs. The following two sections provide a brief description of the single interface surface plasmon; these results are well known in the literature but have been included for completeness and to introduce salient features of these waves.

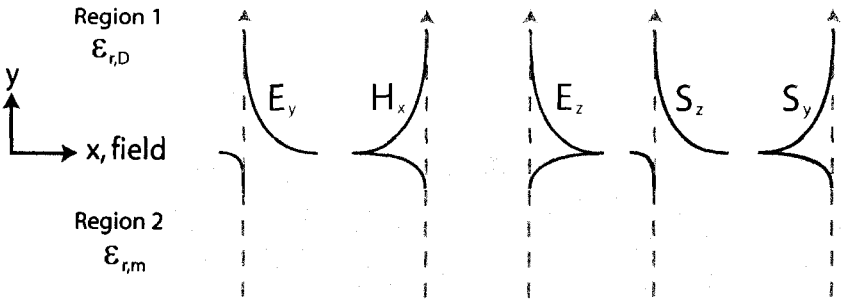

Figure 1-1: Diagram of the metal-dielectric interface along with a sketches of the SPP field components. Relative signs (ie positive and negative) are preserved between the field components (+ to right of gray axis) however the relative magnitudes are not.

1.2 Single-Interface SPP

In this section we will show the field solutions for the single interface SPP mode by deriving them directly from Maxwell's equations. The derivation has been included in the thesis to better understand the surface plasmon in its simplest form before introducing the more complicated 2-dimensional structures, which are discussed in subsequent sections and which have solutions that can only be found numerically.

A diagram of the dielectric and metal regions, along with the co-ordinate system, is shown in Figure 1-1. The relative permittivity of the dielectric and metal regions is given by $\epsilon_{r,D}$ and $\epsilon_{r,m}$ respectively. Experimental observations show that the SPP mode exists as a TM polarized, or p-polarized, wave so we therefore begin our analysis by considering the tangential magnetic field in region i given by $\overline{H_i} = \hat{\mathbf{x}} H_0 e^{-\alpha_{y,i} y} e^{-\gamma_z z}$, where $\gamma_z = \alpha_z + j\beta_z$ and H_0 is the same in both regions since H is continuous across the interface. We assume propagation along the +z axis and a $e^{+j\omega t}$ time dependency. Maxwell's equations in their differential form are:

$$\nabla \times \overline{E} = -j\omega\mu\overline{H} + \overline{M} \tag{1.1}$$

$$\nabla \times \overline{H} = j\omega\epsilon\overline{E} + \overline{J} \tag{1.2}$$

$$\nabla \bullet \overline{E} = \rho/\epsilon \tag{1.3}$$

$$\nabla \bullet \overline{H} = 0 \tag{1.4}$$

In a source free medium the electric and magnetic current densities, given by $\overline{M}$

and $\overline{J}$, along with the electric volume charge density, ρ, are zero. We use Eq. 1.2 to get the electric field components of the TM mode leading to:

$$\overline{E_i} = \hat{\mathbf{y}}\frac{j\gamma_z}{\omega\epsilon_0\epsilon_{r,i}}H_0 e^{(-1)^i\alpha_{y,i}y}e^{-\gamma_z z} + \hat{\mathbf{z}}\frac{(-1)^i j\alpha_{y,i}}{\omega\epsilon_0\epsilon_{r,i}}H_0 e^{(-1)^i\alpha_{y,i}y}e^{-\gamma_z z} \tag{1.5}$$

The transverse wave number, $\alpha_{y,1}$, can thus be found in region 1 by substituting the fields into Eq. 1.1 resulting in

$$\alpha_{y,1} = \sqrt{-\beta_0^2\epsilon_{r,D} - \gamma_z^2} \tag{1.6}$$

and similarly for region 2 we get

$$\alpha_{y,2} = \sqrt{-\beta_0^2\epsilon_{r,m} - \gamma_z^2} \tag{1.7}$$

where $\beta_0 = \sqrt{\omega^2\mu_0\epsilon_0} = 2\pi/\lambda_0$ is the free space wavenumber and $\omega = 2\pi f$ is the angular velocity. By applying the boundary conditions at the interface (y = 0), particularly the condition that tangential electric fields are continuous across a boundary, we arrive at the following condition:

$$\frac{\alpha_{y,1}}{\epsilon_{r,D}} = -\frac{\alpha_{y,2}}{\epsilon_{r,m}} \tag{1.8}$$

Finally, when we combine Eq. 1.6, 1.7 and 1.8 we get propagation constant of the SPP mode:

$$\gamma_z = i\beta_0\sqrt{\frac{\epsilon_{r,m}\epsilon_{r,D}}{\epsilon_{r,m} + \epsilon_{r,D}}} \tag{1.9}$$

Looking at Figure 1-1 we see the fields of the surface mode. Notice how the perpendicular electric field (E_y) changes sign between the metal and dielectric regions

which is a result of $\Re e\{\epsilon_{r,m}\} < 0$. The Poynting vector in the direction of propagation, S_z is actually negative in the metal implying that the power in this region actually propagates in the -z direction while the bulk of SPP mode travels in the +z direction. When the metal is lossy S_y is negative in both regions resulting in a continual power flow downward, into the metal, where it is lost to electron scattering.

1.3 Thin Film

If a metal is made thin enough then the SPP modes from the top and bottom interfaces are able to couple and form super-modes. By applying the method shown above for the three layer system shown in Figure 1-2, with the metal sandwiched between two dielectrics, results in the following transcendental equation.

$$\tanh(t\sqrt{-\gamma_z^2-\beta_0^2\epsilon_{r,m}}) =$$

$$\frac{\epsilon_{r,D1}\sqrt{-\gamma_z^2-\beta_0^2\epsilon_{r,m}}\sqrt{-\gamma_z^2-\beta_0^2\epsilon_{r,D2}}+\epsilon_{r,m}\epsilon_{r,D2}\sqrt{-\gamma_z^2-\beta_0^2\epsilon_{r,D1}}}{\epsilon_{r,D1}\epsilon_{r,D2}(-\gamma_z^2-\beta_0^2\epsilon_{r,m})+\epsilon_{r,m}^2\sqrt{-\gamma_z^2-\beta_0^2\epsilon_{r,D1}}\sqrt{-\gamma_z^2-\beta_0^2\epsilon_{r,D2}}} \tag{1.10}$$

The above equation needs to be solved using a root solving algorithm capable of handling complex numbers, such as Muller's method [8].

This thin film of metal is capable of supporting symmetric, s_b, and asymmetric, a_b, coupled bound modes each with different characteristics. The dependence of the modes' effective index and propagation loss are shown in Figure 1-3 for a Au film with silica claddings above and below (i.e.: $\epsilon_{r,D1} = \epsilon_{r,D2}$). Analysis was performed at a free space wavelength of $\lambda_0 = 1550nm$. The s_b mode does not cutoff as the metal thickness is reduced but rather we see a decrease in the propagation loss along with a decrease in the effective index, which approaches that of the background material indicating that the mode evolves into a plane wave into this material as $t \rightarrow 0$. The a_b mode shows a response of a different nature with fields becoming more highly localized in the metal as the thickness is reduced, which can be seen by the increase in MPA in Figure1-3 (b), where $MPA = -0.02log_{10}(e)\Re e\{\gamma_z\}$ in dB/mm .

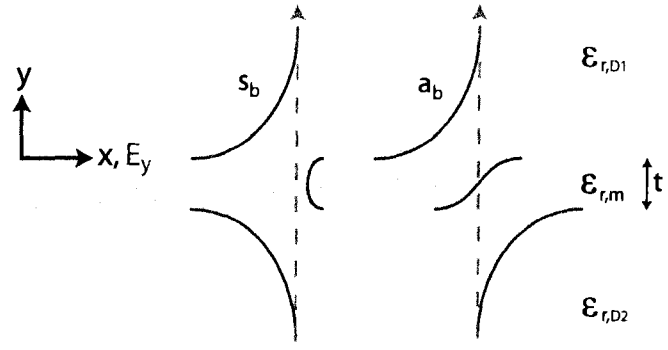

Figure 1-2: Diagram of the thin film structure along with sketches of the field components of the s_b and a_b modes.

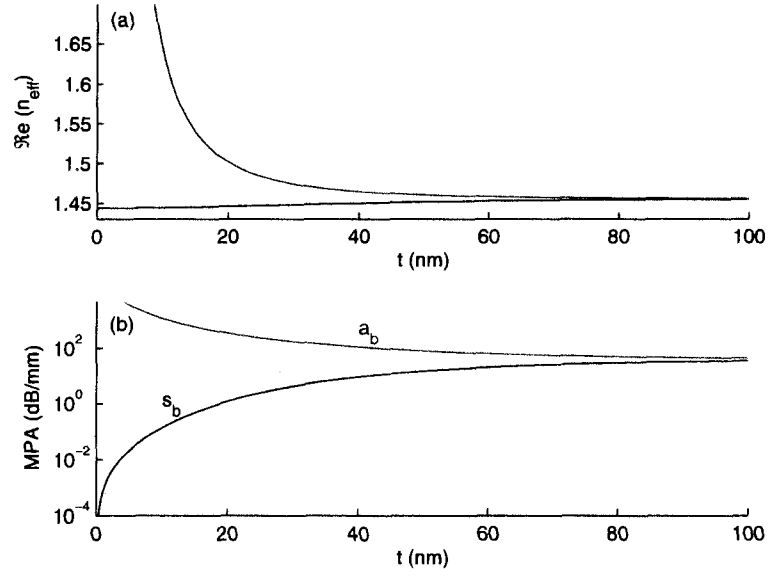

Figure 1-3: (a) Effective index and (b) propagation loss as a function of metal film thickness, t for the s_b and a_b modes. Analysis was performed with silica claddings, $\epsilon_{r,D1} = \epsilon_{r,D2} = 1.444^2$, for a gold film,$\epsilon_{r,m} = -131.95 - 12.65i$ at a free space wavelength of $\lambda_0 = 1550nm$

1.4 Thesis outline

The thesis is assembled as a collection of articles, published or submitted.

Chapter 2 describes a figure of merit study of 2D surface plasmon waveguides which weighs the waveguides' attenuation against its confinement. We look at how changes in dimension and wavelength affect the fundamental long-range mode (ss_b^0) of the metal stripe. The article "as published" in Optics Express is incorporated into the thesis.

Chapter 3 describes a new metallo-dielectric waveguide design, capable of aggressive bends and long-range propagation. This chapter consists of a short paper recently submitted to Optics Letters.

Chapter 4 Provides an in depth analysis of the parallel plate, non-radiative dielectric waveguide and a new metallo-dielectric waveguide at optical frequencies. Various designs are considered in an attempt to optimize the waveguides for long-range propagation and low loss bends.

Chapter 5 has some concluding remarks along with suggestions for future work.

Appendix A consists of a paper convergence analysis of electromagnetic modeling tools applied to some important surface plasmon waveguides. Since convergence was assessed in this paper, a section on this topic was not added to the thesis.

1.5 References

[1] E. Palik, *Handbook of Optical Constants of Solids.* New York: Academic Press, 1985.

[2] A. D. Boardman, *Electromagnetic Surface Modes.* New York: Wiley, 1982.

[3] H. Raether, *Surface Plasmons on Smooth and Rough Surfaces and on Gratings*, ser. Springer Tracts in Modern Physics. New York: Springer-Verlag, 1988, vol. 111.

[4] W. L. Barnes, A. Dereux, and T. W. Ebbesen, "Surface plasmon subwavelength optics," *Nature*, vol. 424, no. 6950, pp. 824–830, 2003.

[5] W. L. Barnes, "Surface plasmon-polariton length scales: a route to sub-wavelength optics," *Journal of Optics a-Pure and Applied Optics*, vol. 8, no. 4, pp. S87–S93, 2006.

[6] S. A. Maier and H. A. Atwater, "Plasmonics: Localization and guiding of electromagnetic energy in metal/dielectric structures," *Journal of Applied Physics*, vol. 98, no. 1, p. 10, 2005.

[7] K. Welford, "Surface-plasmon polaritons and their uses," *Optical and Quantum Electronics*, vol. 23, no. 1, pp. 1–27, 1991.

[8] S. A. Dyer and J. S. Dyer, "Root-finding: Muller's method," *IEEE Instrumentation and measurement magazine*, vol. 3, pp. 38–41, 2000.

Chapter 2

Figures of merit for 2D surface plasmon waveguides and application to metal stripes

My contribution: The paper in this chapter was published in Optics Express and is a follow-up to Dr. Berini's 1-dimensional figure of merit analysis, cited as reference 26 therein. These ideas were adopted and applied to 2-dimensional waveguides. I performed all of the simulation work along with the majority of the analysis of the results. Writing of the paper was split approximately 50/50 between Dr. Berini and myself. The movies in this paper are available online, directly from this open access journal by following: http://www.opticsinfobase.org/abstract.cfm?URI=oe-15-19-12174

Preamble: Three ways of measuring confinement lead to three figures of merit. Depending on the design criteria, one or more of the figures of merit can be used as a quality measure(s) when comparing different waveguides. M_1^{2D} measures confinement based on the mode size which is useful if the size of the mode is a concern (eg. for butt-coupling to a fiber). M_2 measures confinement based on the separation of the mode phase constant (β_z) from the light line, and this gives an indication of how likely it is that the mode will radiate when bent or due to perturbations in and around the waveguide. M_3 measures confinement based on $1/\lambda_g$ and is directly related to the quality factor which is useful when designing resonators.

Figures of merit for 2D surface plasmon waveguides and application to metal stripes

Robin Buckley[1] and Pierre Berini[1,2]

[1]*School of Information Technology and Engineering (SITE), University of Ottawa, 161 Louis Pasteur Ottawa ON, K1N 6N5, Canada*

[2]*Spectalis Corporation, PO Box 72029, Kanata North RPO, Ottawa ON, K2K 2P4, Canada*

pierreberini@spectalis.com, berini@site.uottawa.ca

Abstract: Three figures of merit, useful as quality measures for 2D surface plasmon waveguides, are discussed and applied to help trade-off mode confinement against attenuation for the symmetric mode propagating along metal stripes. Different stripe geometries are considered, and Au, Ag and Al are compared as the stripe metal over the wavelength range from 200 to 2000 nm. Depending on which figure of merit is used, and on how mode confinement is measured, different preferred designs emerge. For instance, given a mode area, narrow thick stripes are better than wide thin ones, but given a distance from the light line, the opposite is true. Each of the metals analyzed show wavelength regions where their performance is best. The figures of merit are generally applicable and should be useful to help compare, assess and optimize designs in other 2D surface plasmon waveguides or in other absorbing waveguides.

OCIS codes: (240.6680) Surface Plasmons; (130.2790) Guided waves.

References and Links

1. M. Bass *et al.*(Editors), "Properties of Metals," in *Handbook of Optics – Vol II*, (McGraw-Hill, 2000).
2. H. Raether, *Surface Plasmons on Smooth and Rough Surfaces and on Gratings* (Springer, Berlin, 1988).
3. K. Welford, "Surface plasmon-polaritons and their uses," Opt. Quantum Electron. **23**, 1-27 (1991).
4. W. L. Barnes, "Surface plasmon-polaritons length scales: a route to sub-wavelength optics," J. Opt. A: Pure Appl. Opt. **8**, S87-S93 (2006).
5. W. L. Barnes, A. Dereux and T. W. Ebbesen, "Surface plasmon subwavelength optics," Nat. **424**, 824-830 (2003).
6. S. A. Maier and H. A. Atwater, "Plasmonics: Localization and guiding of electromagnetic energy in metal/dielectric structures," J. Appl. Phys. **98**, 011101 (2005).
7. D. Sarid, "Long-range surface-plasma waves on very thin metal films," Phys. Rev. Lett. **47**, 1927-1930 (1981).
8. J. J. Burke, G. I. Stegeman, and T. Tamir, "Surface-polariton-like waves guided by thin, lossy metal films," Phys. Rev. B **33**, 5186-5201 (1986).
9. P. Berini, "Plasmon-polariton modes guided by a metal film of a finite width," Opt. Lett. **24**, 1011-1013 (1999).
10. P. Berini, "Plasmon polariton waves guided by thin lossy metal films of finite width: bound modes of symmetric structures," Phys. Rev. B **61**, 10484-10503 (2000).
11. A. Degiron and D. Smith, "Numerical simulations of long-range plasmons", Opt. Express **14**, 1611-1625 (2006).
12. R. Charbonneau, N. Lahoud, G. Mattiussi and P. Berini, "Demonstration of integrated optics elements based on long-ranging surface plasmon polaritons," Opt. Express **13**, 977-984 (2005).
13. R. Charbonneau, C. Scales, I. Breukelaar, S. Fafard, N. Lahoud, G. Mattiussi, and P. Berini, "Passive integrated optics elements based on long-range surface plasmon polaritons," J. Lightwave Technol. **24**, 447-494 (2006).
14. S. Jetté-Charbonneau, R. Charbonneau, N. Lahoud, G. Mattiussi, and P. Berini, "Demonstration of Bragg gratings based on long-ranging surface plasmon polariton waveguides," Opt. Express **13**, 4674-4682 (2005).
15. A. Boltasseva, T. Nikolajsen, K. Leosson, K. Kjaer, M. S. Larsen and S. I. Bozhevolnyi, "Integrated Optical Components Utilizing Long-Range Surface Plasmon Polaritons," J. Lightwave Technol. **23**, 413-422 (2005).
16. A. Boltasseva, S. I. Bozhevolnyi, T. Nikolajsen, and K. Leosson, "Compact Bragg Gratings for Long-Range Surface Plasmon Polaritons," J. Lightwave Technol. **24**, 912-918 (2006).
17. B. Lamprecht, J. R. Krenn, G. Schider, H. Ditlbacher, M. Salerno, N. Felidj, A. Leitner and F.R. Aussenegg, "Surface plasmon propagation in microscale metal stripes," Appl. Phys. Lett. **79**, 51-53 (2001).

#84184 - $15.00 USD Received 15 Jun 2007; revised 3 Sep 2007; accepted 3 Sep 2007; published 10 Sep 2007

18. J.-C. Weeber, J. R. Krenn, A. Dereux, B. Lamprecht, Y. Lacroute, and J.-P. Goudonnet, "Near-field observation of surface plasmon polariton propagation on thin metal stripes," Phys. Rev. B **64**, 045411 (2001).
19. J.-C. Weeber, A. Dereux, C. Girard, J. R. Krenn and J.-P. Goudonnet, "Plasmon polaritons of metallic nanowires for controlling submicron propagation of light," Phys. Rev. B **60**, 9061-9068 (1999).
20. R. Zia, M. D. Selker, P. B. Catrysse and M. L. Brongersma, "Geometries and materials for subwavelength surface plasmon modes," J. Opt. Soc. Am. A **21**, 2442-2446 (2004).
21. K. R. Welford and J. R. Sambles, "Coupled Surface Plasmons in a Symmetric System", J. Mod. Opt. **35**, 1467-1483 (1988).
22. J. A. Dionne, L. A. Sweatlock, H. A. Atwater and A. Polman, "Plasmon slot waveguides: Towards chip-scale propagation with subwavelength-scale localization" Phys. Rev. B **73**, 035407 (2006).
23. I. V. Novikov and A. A. Maradudin, "Channel Polaritons," Phys. Rev. B **66**, 035403 (2002).
24. D. F. P. Pile and D. K. Gramotnev, "Channel plasmon-polariton in a triangular groove on a metal surface," Opt. Lett. **29**, 1069-1071 (2004) http://www.opticsinfobase.org/abstract.cfm?URI=ol-29-10-1069
25. S. I. Bozhevolnyi, V. S. Volkov, E. Devaux, and T. W. Ebbesen, "Channel plasmon-polariton guiding by subwavelength metal grooves," Phys. Rev. Lett. **95**, 046802 (2005).
26. P. Berini, "Figures of merit for surface plasmon waveguides," Opt. Express **14**, 13030-13042 (2006).
27. J. Guo and R. Adato, "Extended long range plasmon waves in finite thickness metal film and layered dielectric materials," *Opt. Express* **14**, 12409-12418 (2006).
28. A. Degiron, C. Dellagiacoma, J. G. McIlhargey, G. Shvets, O. J. F. Martin, and D. R. Smith, "Simulations of hybrid long-range plasmon modes with application to 90° bends," Opt. Lett. **32**, 2354-2356 (2007) http://www.opticsinfobase.org/abstract.cfm?URI=ol-32-16-2354
29. P. Berini, R. Charbonneau, and N. Lahoud, "Long-Range Surface Plasmons on Ultrathin Membranes," Nano Lett. **7**, 1376-1380 (2007).
30. C. Chen, P. Berini, D. Feng, S. Tanev, and V. Tzolov, "Efficient and accurate numerical analysis of multilayer planar optical waveguides in lossy anisotropic media," Opt. Express **7**, 260-272 (2000).
31. I. Breukelaar, R. Charbonneau, and P. Berini, "Long-range surface plasmon-polariton mode cutoff and radiation in embedded strip waveguides," J. Appl. Phys. **100**, 043104 (2006).
32. E. D. Palik (Editor), *Handbook of Optical Constants of Solids*, (Academic Press, Orlando, Florida, 1985).
33. P. Berini, R. Charbonneau, N. Lahoud, and G. Mattiussi, "Characterization of long-range surface-plasmon-polariton waveguides," J. Appl. Phys. **98**, 043109 (2005).

1. Introduction

The optical properties of metals have been studied and are known to exhibit a negative real part of permittivity at optical frequencies [1]. This property allows the metal-dielectric interface to support a surface plasmon-polariton (SPP) mode which is bound to the interface through the coupling of electromagnetic waves to oscillations in conduction electrons in the metal. The SPP has been studied extensively, and has been reviewed by Raether [2], Welford [3], Barnes [4,5], Maier and Atwater [6] among others. The high loss of the single interface SPP makes it, in general, incapable of long range transmission.

A thin metal slab bounded by dielectric supports bound supermodes, labeled s_b and a_b [7,8]. As the thickness of the slab approaches zero the attenuation of the s_b mode, or long-range SPP (LRSPP), decreases and the mode becomes less confined eventually evolving into the TEM wave of the background dielectric. When the width of the thin metal slab is made finite, defining a stripe, and the metal stripe is embedded in a homogeneous background dielectric, then a more complicated set of modes emerge [9,10,11] since the stripe provides 2D confinement in the plane transverse to the direction of propagation. For a sufficiently thin or narrow metal stripe, the ss_b^0 mode becomes long-range (it is the LRSPP). Numerous LRSPP passive devices such as Mach-Zehnder interferometers, Y-junctions, directional couplers [12,13] and Bragg gratings [14], excited by butt-coupling with an optical fiber, have been experimentally tested and shown to closely agree with theory. Similar devices were also reported in [15,16]. The metal stripe exposed to air has also been studied [17-19].

The metal slab and stripe exhibit a trade-off with regards to the confinement and attenuation of the LRSPP supported therein: The confinement and attenuation of the LRSPP rise and fall together [10,20]. This trade-off also applies to other SPP waveguides such as the single-interface, the metal cladded dielectric slab [21,22] and the channel waveguide [23-25], for example. The attenuation-confinement trade-off in surface plasmon waveguides was recently discussed in [26], where three FoMs (figures of merit), denoted M_1^{1D}, M_2 and M_3,

#84184 - $15.00 USD Received 15 Jun 2007; revised 3 Sep 2007; accepted 3 Sep 2007; published 10 Sep 2007

were proposed to assist with trade-off analyses. The FoMs were then used to study three 1D waveguides: the single-interface, the metal slab and the metal cladded dielectric slab [26].

In this paper, we extend the M_1^{1D} FoM proposed in [26] to 2D waveguides, defining the new variant M_1^{2D} (Section 2), and we use the three FoMs (M_1^{2D}, M_2 and M_3) to study the LRSPP in the metal stripe as a function of geometry (Section 3) and metal choice (Au, Ag and Al - Section 4). Section 5 gives a brief summary and conclusions.

2. Figures of merit for 2D waveguides

An $\exp(j\omega t)$ time dependence is assumed with mode propagation occurring along the $+z$ axis with an $\exp(-\gamma_z z)$ dependence, where ω is the angular frequency and $\gamma_z = \alpha_z + j\beta_z$ is the complex propagation constant with α_z and β_z the attenuation and phase constants, respectively. The complex effective index N_{eff} is given by $N_{eff} = \gamma_z/\beta_0 = k_{eff} + jn_{eff}$ where $\beta_0 = 2\pi/\lambda_0$ is the free-space phase constant and λ_0 is the free-space operating wavelength.

2.1 Figures of merit: M_1^{1D}, M_2 and M_3

Three FoMs were defined in [26] to provide objective measures of comparison for purely bound surface plasmon modes in SPP waveguides. Their definition is based on forming benefit-to-cost ratios where the benefit is confinement and the cost is attenuation. Different ways of measuring confinement led to different definitions. The first FoM, $M_1^{1D} = 1/\delta_w\alpha_z$, uses the inverse mode size (δ_w) as its confinement measure, where δ_w is the distance between the $1/e$ field magnitude points of the main transverse electric field component relative to the global field maximum. The second FoM, $M_2 = (\beta_z - \beta_1)/\alpha_z = (n_{eff} - n_1)/k_{eff}$ measures confinement as the mode's distance from the light line in the dielectric. The third FoM, $M_3 = 1/\lambda_g\alpha_z = \beta_z/2\pi\alpha_z = n_{eff}/2\pi k_{eff}$, uses the inverse guided wavelength λ_g as its confinement measure. M_3 is proportional to the quality factor (Q) when dispersion is negligible.

2.2 Definition of the figure of merit M_1^{2D} for 2D waveguides

The definition of M_2, and M_3 holds for modes in 2D waveguides, but the definition of M_1, which is based on mode size, depends on the dimensionality of the structure as emphasized in [26]. For 1D waveguides, the mode size is the width δ_w, leading to M_1^{1D}. For 2D waveguides, the mode size is an area, leading to a new definition for M_1, denoted M_1^{2D}.

The mode size is taken as the area A_e bounded by the closed $1/e$ field magnitude contour relative to the global field maximum. The 2D spatial distribution in the transverse plane of the main transverse electric field component is used to find this contour and the area A_e. The contour and A_e are determined numerically, so highly deformed modes, sometimes supported by SPP waveguides, are easily and unambiguously handled.

Taking the confinement measure as $(\pi/A_e)^{1/2}$, instead of simply $1/A_e$, seems preferable since this measure tends to the inverse mode radius as the mode becomes circular and it leads to a unit-less FoM. This confinement measure also tends to zero as the mode expands or as the waveguide evolves into a 1D structure (as it should since confinement is lost along one of the transverse dimensions). Based on these considerations, the M_1^{2D} FoM is defined as:

$$M_1^{2D} = \sqrt{\frac{\pi}{A_e}}\frac{1}{\alpha_z} \tag{1}$$

3. Geometric study of metal stripe waveguides

The waveguides considered are shown in Fig. 1, and consist of (a) the metal stripe ($w < \infty$) and slab ($w = \infty$), (b) and (c) 2 and 3 symmetrically coupled (SC) metal stripes, and (d) the cladded metal stripe. The cladded metal slab ($w = \infty$) was analyzed in [27], and the cladded metal stripe was recently reported in [28] and added to this paper during revisions. The metal stripe on a thin dielectric layer or membrane (not shown) was recently introduced in [29] and bears points of similarity to the cladded metal stripe [28]. The metal slab was analyzed using the transfer matrix method [30]. A commercial software package based on the finite element

#84184 - $15.00 USD Received 15 Jun 2007; revised 3 Sep 2007; accepted 3 Sep 2007; published 10 Sep 2007

method (Femlab) was used to model the 2D structures. This package has been shown to accurately model surface plasmon waveguides [31]. Only the s_b and ss_b^0 modes are considered and compared. λ_0 was set to 1550 nm, Au was used as the stripe metal ($\varepsilon_{r,m} = -\varepsilon_R - j\varepsilon_I = -131.95 - j12.65$ [32]), with the surrounding dielectric being SiO_2 ($\varepsilon_{r,1} = n_1^2 = 2.085$ [32]) and, additionally, vacuum (ε_0) in the case of the cladded stripe (Fig. 1(d)).

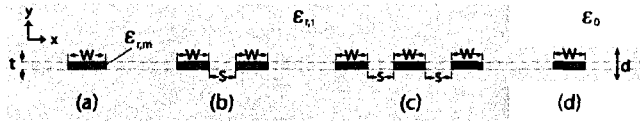

Fig. 1. Cross sectional view of surface plasmon waveguides. (a) Single stripe, (b) pair of SC stripes, (c) three SC stripes, (d) cladded stripe.

The metal stripes (Figs. 1(a)-(c)) are discussed first. Figs. 2(a) and (b) give the effective index (n_{eff}) and attenuation (α_z, k_{eff}) of the s_b and ss_b^0 modes as a function of t. The usual trends of $n_{eff} \rightarrow n_1$ (vanishing confinement) and α_z, $k_{eff} \rightarrow 0$ (vanishing attenuation) as $t \rightarrow 0$ are noted.

Figure 2(c) shows that as t decreases, the mode size increases for all structures considered, as expected. From Fig. 2(d), it is noted that M_1^{1D} and M_1^{2D} increase for all structures as t and/or w decrease, indicating that α_z decreases more rapidly than the modes' expansion. Given a mode size $(A_c/\pi)^{1/2}$, single narrow thick stripes are better than wide thin ones or coupled ones, since they generate less attenuation yielding a larger M_1^{2D}. For a specific t narrower stripes produce a larger M_1^{2D} than wider ones.

The modes' distance from the light line, plotted in Fig. 2(e), decreases with t and w as expected since the modes evolve into the TEM wave of the background as the metal vanishes. From Fig. 2(f) it is noted that M_2 increases sharply with decreasing t, reaching a peak beyond which it tends to 0 as $t \rightarrow 0$. These peaks are located at $t = 18$ nm for the $w = 2$ μm stripe, at $t = 10$ nm for the $w = 8$ μm stripe, at $t = 9.5$ nm for the $wswsw = 22222$ μm SC stripes, and at $t \sim 0$ for the s_b mode in the slab. On the thicker side of the peaks, k_{eff} decreases more rapidly than the confinement ($n_{eff} - n_1$) as t is reduced, but the opposite holds true on the thinner side of the peak. Given a distance from the light line ($n_{eff} - n_1$), single wide thin stripes perform better than narrow thick ones or coupled ones, since they generate less attenuation, yielding a larger M_2. For a specific t wider waveguides produce a larger M_2 than narrower ones. These trends are opposite to those observed from M_1^{2D}.

λ_g plotted in Fig. 2(g) increases with decreasing t and w. M_3, plotted in Fig. 2(h), shows a similar trend to the other FoMs in that M_3 increases with decreasing t. This implies that α_z decreases more rapidly than λ_g increases as t is reduced. Given a t narrower waveguides are better than wider ones leading to a larger M_3, as observed for M_1^{2D}.

The cladded metal stripe (Fig. 1(d)) [28] is similar to the metal stripe on a thin dielectric membrane [29], in that as the thickness of the dielectric changes, the ss_b^0 mode may become more confined and attenuated. Another point of similarity rests with the conditions for ss_b^0 confinement, which are that its n_{eff} must be larger than n_1 and than the n_{eff} of the TM_0 mode in the dielectric slab present to the left and right of the metal stripe. If TM-TE mode conversion is expected, say due to discontinuities, then it should also be larger than the n_{eff} of the TE_0 mode of the dielectric slab, but this condition is essentially otherwise irrelevant as was demonstrated experimentally in [29] since the ss_b^0 and TE_0 modes are substantially orthogonal. In a symmetric slab, the TM_0 and TE_0 modes are guided for all dielectric thicknesses. Another point of similarity rests with the excitation of the waveguides, in that if the source and ss_b^0 mode fields are not well matched then light becomes trapped in the dielectric slab and may interfere with the ss_b^0 mode. This may be problematic in structures such as couplers and Mach-Zehnder interferometers.

#84184 - $15.00 USD Received 15 Jun 2007; revised 3 Sep 2007; accepted 3 Sep 2007; published 10 Sep 2007

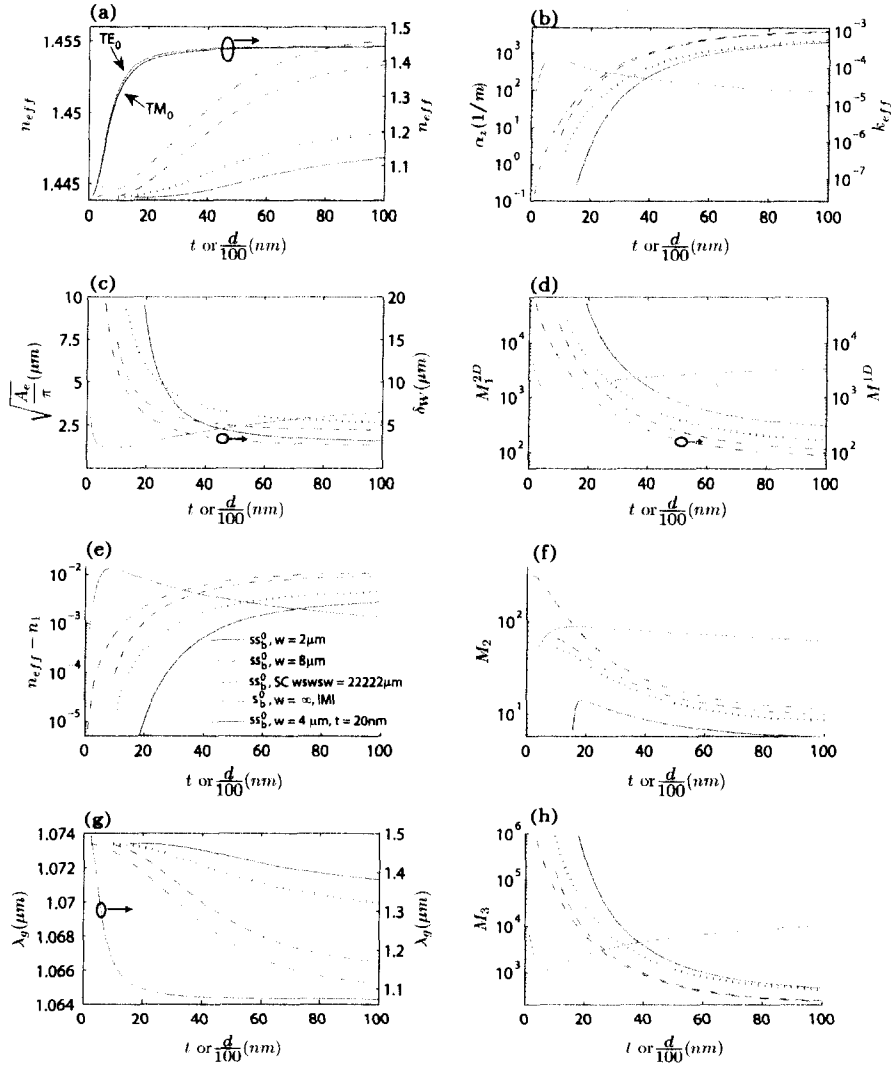

Fig. 2. (a) n_{eff} and (b) α_z and k_{eff} of the ss_b^0 and s_b modes. (c) Mode size for the s_b mode in the slab (right axis) and the ss_b^0 mode in the stripes (left axis). (d) M_1^{1D} (right axis) and M_1^{2D} (left axis). (e) Distance from the light line and (f) M_2. (g) Guided wavelength and (h) M_3. The gray curves are for the cladded stripe (Fig. 1(d)).

Figure 2(a) shows n_{eff} of the ss_b^0 mode in the cladded metal stripe for $w = 4$ μm and $t = 20$ nm, as well as n_{eff} of the TM_0 and TE_0 modes in the dielectric slab alone, as a function of d. From Fig. 2(a) we see that n_{eff} of the ss_b^0 mode is always larger than that of the TM_0 mode, while it falls below that of the TE_0 mode for $d \sim 1.9$ μm. n_{eff} of the ss_b^0 mode decreases as d decreases, which is expected since the mode fields extend further into the vacuum. In Fig. 2(b) α_z increases with d until a maximum, from which it drops quickly. The mode size plotted in Fig. 2(c) decreases with decreasing d until a minimum is reached around $d = 900$ nm. For smaller d the mode extends deeper into the vacuum, explaining the decreasing α_z and n_{eff}.

#84184 - $15.00 USD Received 15 Jun 2007; revised 3 Sep 2007; accepted 3 Sep 2007; published 10 Sep 2007

Indeed, the mode tends toward cut-off ($n_{eff} \sim n_1$) in this region. M_1^{2D} plotted in Fig. 2(d) decreases with decreasing d, implying that α_z increases more rapidly than the confinement measured as the mode size, until $d \sim 675$ nm beyond which the opposite trend holds. The distance from the TM_0 mode is plotted in Fig. 2(e) instead of the distance from the light line, i.e.: n_{eff} of the TM_0 mode is used instead of n_1 since it is larger. The corresponding M_2 plotted in Fig. 2(f) increases with decreasing d up to a peak at $d \sim 1.67$ μm, indicating that the confinement measured as this distance increases more rapidly than k_{eff}. Decreasing d decreases λ_g as shown in Fig. 2(g). The corresponding M_3 plotted in Fig. 2(h) shows a similar trend to M_1^{2D}, decreasing with d until $d \sim 650$ nm.

It is noted that M_1^{2D}, M_2 and M_3 of the cladded metal stripe (Fig. 1(d)) are larger than those of the metal stripe (Fig. 1(a), $d = \infty$) over a good range of dimensions, indicating that the former can provide a better trade-off between confinement and attenuation, as noted in [28]. It must be borne in mind, however, that the metal stripe must have a smaller t or w or both as d decreases in order to maintain the same α_z and thus the same range as the $d = \infty$ case. Producing high quality metal stripes can be challenging for $t < 20$ nm [33].

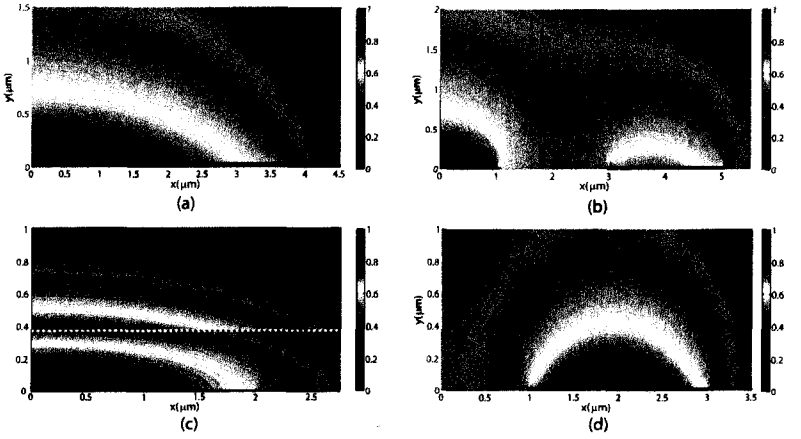

Fig. 3. Spatial distribution of $|E_y|$ associated with the ss_b^0 mode in various waveguides. Quarter symmetry is used with the origin, ($x = y = 0$), being the center of the mode. The 1/e field contour is also plotted as the thin black curve. In all cases, the fields are normalized such that $\max(|E_y|) = 1$. (a) Single stripe with $w = 8$ μm and $t = 70$ nm; the associated movie shows a sweep over t. (b) Three SC stripes with $wswsws = 22222$ μm and $t = 70$ nm; the associated movie shows a sweep over t. (c) Cladded stripe with $w = 4$ μm, $t = 20$ nm and $d = 0.8$ μm; the associated movie shows a sweep over d. (d) Pair of SC Au stripes, $wsw = 222$ μm, $t = 30$ nm and $\lambda_0 = 1000$ nm; the associated movie shows a sweep over λ_0.

Figures 3(a), (b) and (c) give the spatial distribution of $|E_y|$ associated with the ss_b^0 mode in a single stripe having $w = 8$ μm and $t = 80$ nm, in three SC stripes having $wswsw = 22222$ μm and $t = 70$ nm and in a cladded stripe having $w = 4$ μm and $t = 20$ nm, respectively. The $1/e$ field contour is plotted as the thin black curve and the SiO_2-vaccuum interface is shown as the dashed white line in Fig. 3(c). There is also an inner contour(s) that exists near the surface of the stripe(s), which depends on the penetration of $|E_y|$ into the metal. In the case of Figs. 3(a) and (c), the area A_c is the area within the outer closed contour, not including the area within the inner closed contour since the field enclosed by the latter has a magnitude below the $1/e$ level. The movies associated with Figs. 3(a) and (b) show how the mode evolves with t. Both waveguides show the field and $1/e$ contour extending further into the dielectric as t is reduced. This decrease in confinement also causes the mode field to become more circular, more closely matching that of a single mode fiber. This can be seen in the movie in Fig. 3(a) with the mode field almost circular for $t \leq 20$ nm. From the movie in Fig. 3(b), weaker coupling

#84184 - $15.00 USD Received 15 Jun 2007; revised 3 Sep 2007; accepted 3 Sep 2007; published 10 Sep 2007

between the three SC stripes is observed from the shape of the mode field as t and the confinement increase. The movie in Fig. 3(c) shows the mode size decreasing with d until $d \sim$ 900 nm where the $1/e$ field begins to extend further into the vacuum region.

4. Wavelength response of metal stripe waveguides

The FoMs are now used to assess the wavelength response of metal stripe waveguides for three different metals embedded in SiO_2: Ag, Au and Al. The optical properties of these materials were taken from the experimentally determined data compiled in Palik [32]. A cubic spline was used to interpolate the permittivity at the desired wavelengths. The waveguides used in the analysis were chosen based on their similar proximity to the light line at $\lambda_0 = 1550$ nm (all have $n_{eff} - n_1 \sim 5\times10^{-4}$, Fig. 2(e)): A single stripe with $w = 2$ μm, $t = 40$ nm, a single stripe with $w = 4$ μm, $t = 20$ nm, and a pair of SC stripes with $wsw = 222$ μm, $t = 30$ nm.

Figure 4(a) shows n_{eff} versus λ_0 of the ss_b^0 mode, along with the light line in SiO_2; Fig. 4(b) shows the corresponding α_z. An interesting feature arose in the case of Au: n_{eff} of the single interface SPP crosses the light line at $\lambda_0 = 473$ nm (slightly beyond the energy asymptote), while n_{eff} of the slab and of the stripes do not cross the light line at this wavelength. The modes appear to remain bound for $\lambda_0 \geq 250$ nm. This trend does not show up in the case of Ag. The modes supported by the Al waveguides did not reach their energy asymptote for the range of wavelengths used, which makes it unclear as to whether Al would show this feature. Fig. 4(b) shows that lower loss can be achieved when operating deeper into the infrared for all the waveguides and metals analyzed. For all metals, as the wavelength decreases, the ss_b^0 mode becomes more localized to the center of the stripe along the metal/dielectric interfaces and the effects of the corners and the dielectric regions on either side diminish.

Figure 4(c) shows that the mode size increases when operating further into infrared. At short wavelengths the curves exhibit features and small peaks which are explained by inspecting the mode fields, revealing that they increase in strength near the corners at specific wavelengths. This behavior also perturbs the $1/e$ contour associated with the modes.

Figure 4(d) shows that M_1^{2D} increases with increasing wavelength, whereas M_1^{1D} remained flat in the Drude region as observed from Fig. 3 of [26]. The modes supported by the Ag waveguides experience a small drop in M_1^{2D} near $\lambda_0 = 1630$ nm while the Al waveguides show a drop for λ_0 between 700 and 900 nm. Looking at Fig. 4(b), an increase α_z is observed in these regions, which is not matched by an equivalent increase in confinement, causing the dip in M_1^{2D}. In the wavelength range around 1630 nm, where the Ag structures show a decrease in M_1^{2D}, Au out-performs. Al is a good choice for $\lambda_0 \leq 400$ nm.

From Fig. 4(e) it is noted that the distance from the light line decreases sharply at long wavelengths. Interestingly, M_2 plotted in Fig. 4(f), exhibits maxima for Au and Ag. The Ag structures exhibit a peak with its location depending slightly on the geometry: the $w = 4$ μm $t = 20$ nm, $wsw = 222$ μm $t = 30$ nm, and $w = 2$ μm $t = 40$ nm structures have peaks at $\lambda_0 = 845$, 835 and 825 nm, respectively. The corresponding Au structures also exhibit peaks in M_2 near these wavelengths, but they are broader and lower than those of the Ag structures. Ag outperforms Au over a broad wavelength range but beyond 1630 nm Au seems better. M_2 decreases sharply on the long wavelength side of the peak, in keeping with the rapid loss of confinement noted earlier from Fig. 4(e). Based on M_2, it is preferable to operate Au and Ag waveguides near the short wavelength limit of the Drude region, as was already observed for Ag in [26]. The modes supported by the Al waveguides show a decrease in M_2 for λ_0 in the range of 400 to 900 nm. The Al waveguides again perform better than the Au and Ag ones for $\lambda_0 \leq 400$ nm, while being considerably outperformed throughout the rest of the spectrum.

Figure 4(f) shows the quality factor Q. (In the calculation of Q, the derivative in Eq. (18) of [26] was estimated using finite difference approximants.) M_3 is shown in Fig. 4(h). When the modes experience minimal dispersion, as they do in the Drude region, then $Q \sim \pi M_3$, as is observed by comparing these Figs. In the short wavelength region the modes experience a large change in their n_{eff} as they approach the energy asymptote, causing a greater difference between Q and M_3. Both sets of curves show a similar trend to M_1^{2D}, where the Au and Ag

#84184 - $15.00 USD Received 15 Jun 2007; revised 3 Sep 2007; accepted 3 Sep 2007; published 10 Sep 2007

structures outperform the Al ones for $\lambda_0 \geq 400$ nm. Silver outperforms Au for $\lambda_0 \geq 400$ nm until about 1630 nm, where Au appears to be better.

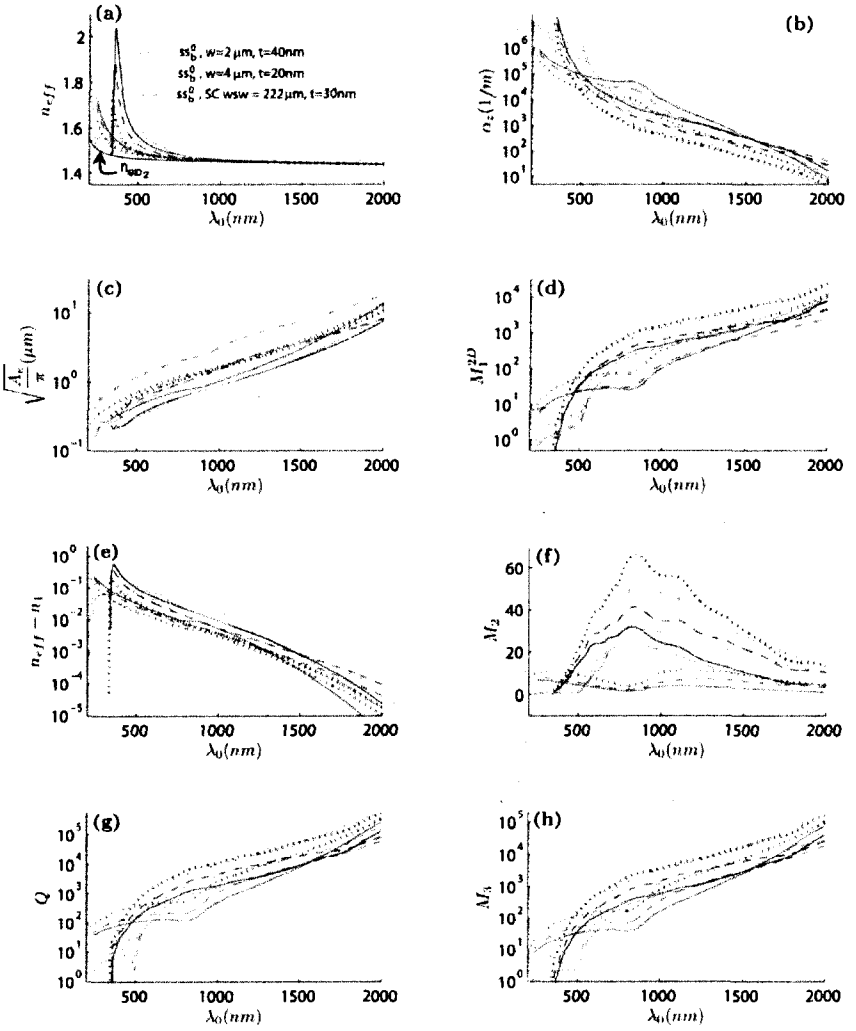

Fig. 4. (a) n_{eff} and (b) α_z versus λ_0. (c) Mode size and (d) M_1^{2D}. (e) Distance from the light line and (f) M_2. (g) Quality factor Q and (h) M_3. (green: Au, blue: Ag, magenta: Al)

Figure 3(d) gives the spatial distribution of $|E_y|$ associated with the $ss_b^{\ 0}$ mode in two SC Au stripes having $wsw = 222$ μm and $t = 30$ nm. The associated movie shows how the mode evolves with decreasing λ_0. As the mode approaches its energy asymptote, it becomes more confined and localized to the center of the stripe along the metal/dielectric interfaces. At short λ_0, the coupling between the stripes weakens, eventually disappearing altogether.

#84184 - $15.00 USD Received 15 Jun 2007; revised 3 Sep 2007; accepted 3 Sep 2007; published 10 Sep 2007

5. Summary and concluding remarks

The FoM M_1^{2D} was defined for 2D waveguides as the ratio of $(\pi/A_e)^{1/2}$ to α_z.. Using this FoM, along with those proposed in [26], a quantitative comparison of metal stripe waveguides supporting the ss_b^0 mode was performed as a function of stripe geometry, stripe metal and λ_0, assuming SiO_2 as the background dielectric. Depending on how confinement is measured, and thus on which FoM is used, then different conclusions on waveguide quality are reached.

Various geometries were considered for Au stripes at $\lambda_0 = 1550$ nm. The analysis showed that, for a given t, narrower single stripes maximize both M_1^{2D} and M_3, while M_2 is maximized by wider single stripes. Also, given a mode area, single narrow thick stripes are better than wide thin ones or coupled ones, according to M_1^{2D}. M_2 yields an opposite result, where given a distance from the light line, single wide thin stripes are better than narrow thick ones or coupled ones.

The cladded metal stripe was also considered, yielding larger FoMs over a good range of dimensions and hence a better confinement-attenuation trade-off than the stripe. It was noted though that in order to match the range of the stripe, the metal thickness and/or width needed to be decreased, which could challenge fabrication.

The wavelength response of various structures was computed for Au, Ag and Al as the stripe. Operating at longer wavelengths maximizes M_1^{2D} and M_3, in contrast to M_1^{1D} which remained flat [26]. M_2 exhibits well-defined maxima for Au and Ag at $\lambda_0 \sim 850$ nm (near the short wavelength limit of the Drude region), varying slightly depending on the geometry. Based on all of the FoMs, Al provides the best performance for $\lambda_0 \leq 400$, with Au possibly being better for $\lambda_0 > 1630$ nm and Ag performing better throughout the rest of the spectrum. These conclusions, which depend on the measured optical parameters of the metals collected in [32], should also hold for other 2D SPP waveguides (e.g.: [23-25]).

#84184 - $15.00 USD Received 15 Jun 2007; revised 3 Sep 2007; accepted 3 Sep 2007; published 10 Sep 2007

Chapter 3

Long-Range Substantially Non-Radiative Metallo-Dielectric Waveguide

My contribution: The concept for this new metallo-dielectric waveguide (MDW) was introduced by Dr. Berini, who also generated preliminary modelling results. Using the Method of lines and COMSOL I performed simulations and contributed ideas toward the optimization of the designs. Since the waveguide showed excellent performance the results were gathered for the paper in this chapter, recently submitted to Optics Letters. I produced all of the results in this paper and wrote the first draft of the article which was followed by ideas and revisions from Dr. Berini.

Preamble: This chapter gives a short introduction to the metallo-dielectric waveguide; its low loss and non-radiative characters are highlighted and shown through simulations. The new waveguide concept was inspired by the non-radiative dielectric waveguide, which works well at microwave frequencies but appears to be less effective at optical frequencies due to excitation of SPPs.

Long-Range Substantially Nonradiative Metallo-Dielectric Waveguide

Robin Buckley,[1,*] and Pierre Berini [1,2]

[1] *School of Information Technology and Engineering SITE, University of Ottawa*

161 Louis Pasteur, Ottawa ON, K1N 6N5, Canada

[2] *Spectalis Corporation*

PO Box 72029, Kanata North RPO, Ottawa ON, K2K 2P4, Canada

[*] *Corresponding author: rbuck061@uottawa.ca*

A new waveguide structure capable of aggressive bends ($r_0 \rightarrow 0$) and long-range propagation ($\sim 1.2dB/mm$) is described here. The structure uses a step index slab to create the vertical confinement and a pair of metallic parallel plates on either side of the core for lateral confinement. The parallel plates are dimensioned to ensure that all modes which would cause radiation loss in a bend are cut-off.

OCIS codes: 350.5500, 310.6805, 250.5403, 230.2090.

The ability to guide and redirect optical energy is a fundamental requirement in any optical system or component. Dielectric waveguides can sustain a well confined mode, which is virtually lossless, however, they are unable to undergo aggressive 90^0 bends ($r_0 \rightarrow 0$) without becoming highly radiative [1–5]. Surface plasmon polariton (SPP) waveguides can also be designed to produce sharp bends but at the expense of increased propagation loss. This is due to the fact that SPP waveguides have two mutually exclusive properties [6]; one can have a SPP mode that is either long-range with low confinement which radiates when bent too aggressively [7–11] or that is well confined with high attenuation and is able to undergo sharp bends [12–16]. Years ago Yoneyama and Nishida introduced a non-radiative dielectric (NRD) waveguide [17, 18], shown in Fig. 1 (a), for use at microwave frequencies, a structure that has been worked on substantially over the years to produce many microwave integrated circuit devices [19,20], but recent analysis of this structure at optical frequencies [21] reveals the modes to be highly attenuated. Retaining the concept of using metallic plates to suppress radiation we describe here a long-range ($\sim 1.2dB/mm$) substantially nonradiative metallo-dielectric waveguide (MDW) that is capable of aggressive bending ($r_0 \rightarrow 0$), attributes that together have heretofore only been known to exist in some photonic crystal structures [22]. Ease of fabrication along with optoelectronic/electro-optic capabilities are potential additional advantages offered by the MDW.

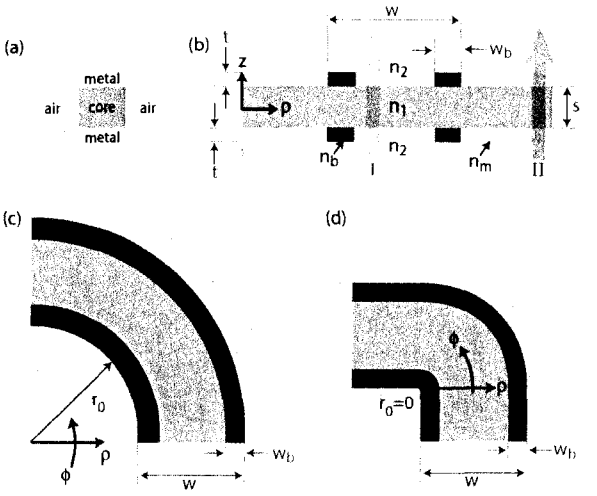

Fig. 1. (a) Cross sectional view of the NRD waveguide along with the MDW design shown in (b) cross-sectional view, (c) top view with an arbitrary radius of curvature r_0, and (d) top view for $r_0 = 0$.

The MDW design is shown in both the cross-sectional view, Fig. 1 (b), and the top view, Fig. 1 (c) and (d). Since the waveguide supports families of quasi TE and TM modes we adopt the nomenclature used to identify rectangular dielectric waveguide modes suggested by Marcatili [23], with the fundamental quasi TE and TM modes identified as E_{11}^{ρ} and E_{11}^{z} respectively. The structure is investigated at a free space operating wavelength of λ_0=1550nm. The core layer is assumed to be an isotropic dielectric of index $n_1 = 2.1375$, representative of high index materials (e.g.: Si_3N_4) and electro-optic crystals (e.g.: $LiNbO_3$, $PLZT$). The upper and lower claddings are assumed to have an index of $n_2 = 1.444$, representative of SiO_2 and optical polymers. Lateral confinement is provided by thin gold ($n_m = \sqrt{-131.95 - 12.65i}$) films of thickness t=100nm, forming two metallic parallel plate waveguides separated by w. High index (n_b=3.4757) plugs, having a width of $w_b = 200$nm, are placed at the edge of the metal layers.

1D slab analysis along the core and the parallel plates, as shown in Fig. 1 (b) by the blue and purple arrows labeled I and II respectively, was conducted first to gain insight on the operation of the waveguide. Computations for the 1D systems were performed using the Transfer Matrix Method [24]. The metal layers were assumed semi-infinite in thickness,because at λ_0=1550nm the field penetration depth in the metal is negligible compared to $t = 100nm$. Fig. 2 shows the effective index of the TE and TM modes that exist in the dielectric core (blue curves) and the parallel plates (purple curves). The refractive index of the core, n_1, and the cladding, n_2, are also plotted in Fig. 2 along with the effective index of the single interface SPP guided along the $Au - n_2$ interface, $n_{eff} = \Re e\{\sqrt{(n_2^2 * n_m^2)/(n_2^2 + n_m^2)}\}$, in Fig 2 (b). Vertical confinement is achieved by a step index dielectric slab; as long as the effective index of the fundamental TE_0 mode remains above that of plane waves in n_2 the mode remains guided. The mechanism for lateral confinement is similar

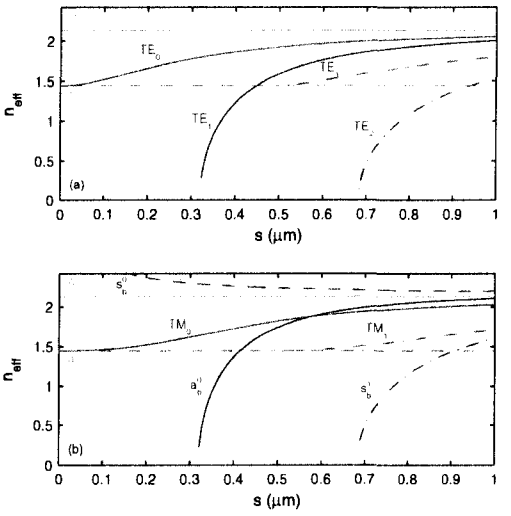

Fig. 2. Effective index as a function of core thickness, s, for two 1D slab waveguides. The slab waveguide represented by the blue curves is made up of $n_2 - n_1 - n_2$, region I in Fig. 1 (a), while the purple curves represent a $Au - n_1 - Au$ parallel plate waveguide, region II in Fig. 1 (a) (the n_2 and Au layers extend to infinity). The (a) TE and (b) TM modes are shown here along with the index n_1, n_2 and the effective index of the single interface SPP at the $Au - n_2$ interface.

except that confinement is assessed with respect to the modes of the parallel plate waveguides instead of plane waves. Fig. 2 (a) shows that the effective index of the fundamental TE_0 mode remains above those of the parallel plate TE_1, TE_2,...etc modes. Its effective index also remains above those of the TM modes (SPP at the $Au - n_2$ interface, a_b^0 and s_b^1), which are shown in Fig. 2 (b). The plasmonic s_b^0, a_b^0 and s_b^1 modes evolve from the TEM, TM_1 and TM_2 modes of a parallel plate waveguide constructed from perfect electric conductors (PECs). Although the effective index of the s_b^0 mode is higher than that of the TE_0 mode essentially no coupling is anticipated due to orthogonality. The MDW is therefore expected to produce both vertical and horizontal confinement in the core for any thickness, s. Furthermore, if a thickness of $s \leq 300$nm is chosen, tight radii of curvature, r_0, should be achievable since all the parallel plate modes are cut off, leaving only the orthogonal s_b^0 mode. Based on this analysis the thickness, s, should be chosen for aggressive bends based on two criteria: 1) single mode operation of the fundamental TE mode and 2) cutoff of as many parallel plate modes as possible.

The 2D straight ($r_0 = \infty$) structure was then modeled in rectangular coordinates using the finite element method (Comsol [25]) and the method of lines [8]. In an attempt to reduce the propagation loss of the E_{11}^{ρ} mode small dielectric regions of both high and low refractive index were placed strategically in many different locations. In the end, it was found that when high index plugs were added to the end of the metal layers (of index n_b, see Fig 1), the propagation loss was reduced by approximately an order of magnitude. Fig. 4 (a) shows the main field component of this mode. By making the width $w = 1.7\mu$m single-mode operation is

ensured along the ρ-axis. At this width, the mode exhibits a propagation loss of 31.25dB/mm, which is too high to travel large distances. Increasing the width to $w = 5\mu$m produces a substantial drop in propagation loss, down to 1.23 dB/mm. When designing components, wider straight sections could be used to propagate the mode over long distances; then an aggressive taper could be inserted to reduce the width to a narrower single-mode section before bending the waveguide.

Fig. 3 shows the computed bending results for two MDW designs, and a rectangular dielectric waveguide consisting of a core, n_1, embedded in a cladding, n_2, having a thickness, $s = 300nm$ and a width narrow enough to ensure single mode operation. One of our waveguide designs was chosen with a thickness of $s = 300nm$ and the other with a thicker core, $s = 500nm$ in order to show the losses due to radiation into parallel plate modes. These results were generated using the Method of Lines in cylindrical co-ordinates [9]. The design with the thicker core is outperformed by the dielectric waveguide, but our thin core design shows better performance with a calculated insertion loss of only $0.61\text{dB}/90^0$ at $r_0 = 150nm$, producing substantially less loss than the dielectric waveguide at small r_0. The computations do not go to $r_0 = 0$ because of numerical limitations but the insertion loss is expected to remain low for $r_0 \rightarrow 0$ as the trend suggests. The inset to Fig. 3 (a) shows a narrow region with increased loss at $r_0 = 1.8\mu$m. Inspection of the fields in this vicinity indicates that there is a resonance occurring, where optical energy is transfered into the dielectric plugs. The low radiation loss in the plane of the waveguide confers other advantages such as allowing short nonradiative tapers. This allows for a quick transition between wider low loss sections and narrower single mode sections.

In Fig. 4 (a) the main TE field component of the E^{ρ}_{t1} mode is shown for a straight waveguide ($r_0 = \infty$). Figs 4 (b) and (c) shows the field distributions for the design with $s = 300$nm, bent at $r_0 = 400$ nm. No radiation exists inside the parallel plate section; only a small amount of leakage occurs into single interface SPP modes at the upper/lower Au/n_2 interface, as apparent in (c), and into plane waves above and below the metal claddings. (d) and (e) shows the field distribution of the E_ρ and E_z fields for the design with a thicker core, s=500nm, indicating clearly that radiation is leaking into the a^0_b and s^1_b modes of the parallel plate waveguide. A transition loss is expected at the junction between straight and bent waveguide sections since mode field deformation occurs as r_0 is reduced, as is apparent by comparing Fig. 4 (a) and (b). Computation of the overlap integral between these two modes revealed that a ~300nm offset reduced the transition loss to <1dB, as compared to 3.6dB with no offset.

In conclusion, we have introduced a long-range MDW capable of propagating along bends with small radius of curvature. By removing most of the radiation channels, the waveguide can be bent with $r_0 \rightarrow 0$ while having virtually no loss. Straight propagation is also possible with relatively low loss (1.23 dB/mm) by flaring out the waveguide width. Electro-optic or optoelectronic functions could be integrated into the

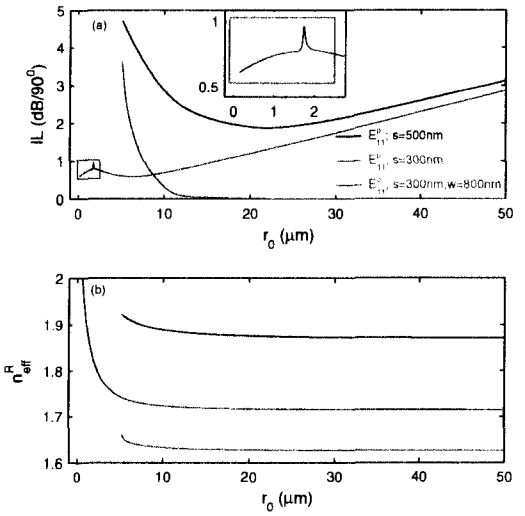

Fig. 3. (a) Insertion loss through a 90^0 bend and (b) effective index, $\mathrm{Re}\{n_{eff}\}$, as a function of the radius of curvature, r_0. The **black** and blue curves represent metallo-dielectric waveguide with different core thicknesses, s, and the magenta curve represents a rectangular dielectric waveguide with thickness s and width w, for comparison.

design as the metallic plates provide ideal noninvasive contacts.

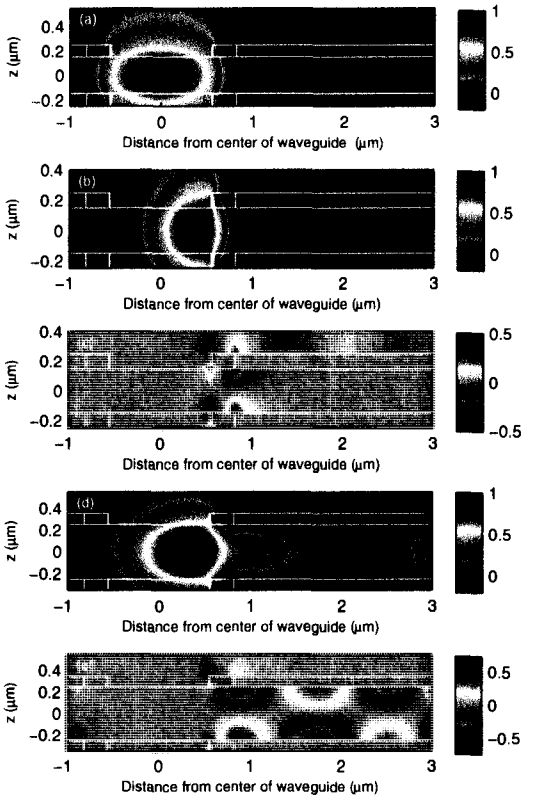

Fig. 4. E_{11}^{ρ} Mode fields with the waveguide outline drawn in white. (a) Main transverse electric field E_ρ for a straight waveguide (w=1.7μm, s=300nm, t=100nm, $r_0 = \infty$). (b) E_ρ and (c) E_z for a bent waveguide (w=1.7μm, s=300nm, t=100nm, r_0=0.4μm) having s such that all parallel plate modes are cutoff except the s_b^0 mode, which is guided to s=0. (d) E_ρ and (e) E_z for a bent waveguide (w=1.7μm, s=500nm, t=100nm, r_0=5.15μm) with s chosen such that the a_b^0 and s_b^1 modes are not cut off.

References

1. R. L. Espinola, R. U. Ahmad, F. Pizzuto, M. J. Steel, and R. M. Osgood, Opt. Express **8**, 517 (2001).
2. M. Popovic, K. Wada, S. Akiyama, H. A. Haus, and J. Michel, J. Lightwave Technol. **20**, 1762 (2002).
3. B. M. A. Rahman, D. M. H. Leung, S. S. A. Obayya, and K. T. V. Grattan, Appl. Optics **47**, 2961 (2008).
4. A. Sakai, G. Hara, and T. Baba, Jpn. J. Appl. Phys. 2 **40**, L383 (2001).
5. Y. A. Vlasov and S. J. McNab, Opt. Express **12**, 1622 (2004).
6. P. Berini, Opt. Express **14**, 13030 (2006).
7. P. Berini, J. Appl. Phys. **102**, 053105 (2007).
8. P. Berini, Phys. Rev. B **61**, 10484 (2000).
9. P. Berini and J. Lu, Opt. Express **14**, 2365 (2006).
10. A. Degiron, S. Y. Cho, C. Harrison, N. M. Jokerst, C. Dellagiacoma, O. J. F. Martin, and D. R. Smith, Phys. Rev. A **77**, 021804 (2008).
11. A. Boltasseva, T. Nikolajsen, K. Leosson, K. Kjaer, M. S. Larsen, and S. I. Bozhevolnyi, J. Lightwave Technol. **23**, 413 (2005).
12. D. F. P. Pile and D. K. Gramotnev, Opt. Lett. **29**, 1069 (2004).
13. G. Veronis and S. H. Fan, Appl. Phys. Lett. **87**, 3 (2005).
14. A. V. Krasavin and A. V. Zayats, Appl. Phys. Lett. **90**, 211101 (2007).
15. S. I. Bozhevolnyi, V. S. Volkov, E. Devaux, J. Y. Laluet, and T. W. Ebbesen, Nature **440**, 508 (2006).
16. B. Steinberger, A. Hohenau, H. Ditlbacher, A. L. Stepanov, A. Drezet, F. R. Aussenegg, A. Leitner, and J. R. Krenn, Appl. Phys. Lett. **88**, 94104 (2006).
17. T. Yoneyama and S. Nishida, IEEE T. Micro. Theory **29**, 1188 (1981).
18. T. Yoneyama, in *Infrared and millimeter waves. Vol.11. Millimeter components and techniques, part III* (Academic Press, 1984), pp. 61–98.
19. T. Yoneyama and S. Nishida, Int. J. Infrared Milli. **4**, 439 (1983).
20. T. Yoneyama, H. Sawada, and T. Shimizu, IEICE T. Electron. **E90C**, 2170 (2007).
21. F. Kusunoki, T. Yotsuya, J. Takahara, and T. Kobayashi, Appl. Phys. Lett. **86**, 211101 (2005).
22. A. Mekis, J. C. Chen, I. Kurland, S. Fan, P. R. Villeneuve, and J. D. Joannopoulos, Phys. Rev. Lett. **77**, 3787 (1996).
23. E. A. J. Marcatili, Bell Tech. J. **48**, 2071 (1969).
24. C. K. Chen, P. Berini, D. Z. Feng, S. Tanev, and V. P. Tzolov, Opt. Express **7**, 260 (2000).
25. COMSOL, *Electromagnetic Module* (2005). V3.2.

Chapter 4

Radiation Suppressing Metallo-Dielectric Optical Waveguides

My contribution: Modelled the optical performance of the parallel-plate waveguide, the non-radiative dielectric (NRD) waveguide and the new metallo-dielectric waveguide (MDW) described in the previous chapter. Through 1D and 2D analyses I attempted to optimize the NRD and MDW structures in order to compare their performance. I generated all of the results in this paper and wrote the article with revisions and ideas from Dr. Berini.

Preamble: This chapter looks at the design characteristics of the non-radiative dielectric and metallo-dielectric waveguide. Each waveguide is compared against a high-confinement dielectric waveguide to see if its low loss and low radiation bends can be can be improved upon.

Radiation Suppressing Metallo-Dielectric Optical Waveguides

Robin Buckley, *Student Member, IEEE,* and Pierre Berini, *Senior Member, IEEE, Member, OSA*

Abstract

A theoretical study of the optical performance of the parallel-plate waveguide, the non-radiative dielectric (NRD) waveguide and the recently proposed metallo-dielectric waveguide (MDW) is reported. One dimensional analysis is used to gain insight into their operation, followed by full-wave 2D simulations of the waveguides in their straight and curved form. The modes supported by the NRD waveguide appear to be spoiled by the excitation of SPPs along the metal surface causing high propagation loss for the straight waveguide and mode deformation along radial bends, as $r_0 \rightarrow 0$. The MDW shows promising results due to its ability for long-range propagation ($\sim 1.2dB/mm$) and low loss bends. The waveguide also has potential use in optoelectronic/electro-optic components due to the presence of the metal plates.

Index Terms

Waveguide bends, nonradiative dielectric waveguides, modeling, optical waveguide theory, plasmons.

I. Introduction

One of the fundamental difficulties in creating optical systems or components lies in the simple notion of redirecting optical energy. Dielectric waveguides can provide a nearly lossless means for mode confinement but become radiative when bent aggressively, as $r_0 \rightarrow 0$ [1]–[5]. One alternative is to use surface plasmon polariton (SPP) waveguides which can be designed for aggressive bends. But this comes at the expense of increased propagation loss due to the direct relation between confinement and attenuation [6], limiting SPP waveguides to either be designed to support a long-range mode with low confinement which radiates when bent [7]–[16] or a well confined mode with high attenuation which can be bent aggressively without radiating [17]–[22].

Robin Buckley is a Candidate for M.A.Sc. in Electrical Engineering at the University of Ottawa

Pierre Berini is associated with Spectalis Corporation, PO Box 72029, Kanata North RPO, Ottawa ON, K2K 2P4, Canada

P. Berini and R. Buckley are with the School of Information Technology and Engineering SITE, University of Ottawa, 161 Louis Pasteur, Ottawa ON, K1N 6N5, Canada

Manuscript received

Highly confined modes are achievable with the parallel-plate waveguide, which is an interesting structure in and of itself. Its electromagnetic characteristics are well-known at microwave frequencies [23], where metals can readily be modeled as perfect electric conductors (PECs). At optical wavelengths metals no longer resemble a PEC, but rather have a negative real part of permittivity ($\Re e\{\epsilon_{r,m}\} < 0$). A TM polarized SPP is supported at a the metal-dielectric interface [24]. At optical wavelengths the parallel plate waveguide supports a similar set of guided modes [25], [26] although they are perturbed from the PEC solutions [23]. This parallel plate or gap waveguide has been studied substantially [27]–[31] due to its ability for subwavelength confinement and high energy localization.

The parallel plate offers 1D confinement only, but variations thereof can provide confinement along the remaining transverse dimension. The Non-Radiative Dielectric (NRD) waveguide for example, introduced for use at microwave frequencies by Yoneyama and Nishida [32]–[35], provides 2D confinement. At microwave frequencies the NRD retains the inherent low-loss characteristics of the dielectric waveguide while eliminating virtually all possible radiation channels, making the waveguide ideal for sharp radial bends ($r_0 \rightarrow 0$). Although at optical frequencies this waveguide cannot be considered "dielectric" we retain the name herein for consistency with the literature. Similar structures have been studied at optical frequencies with confinement being achieved through index guiding limiting the beam divergence of the parallel plate [36], along with another design capable of guiding by means of a low refractive index core [37]. Both of these structures exhibit high loss comparable to similar SPP waveguides (eg.: [17]–[22]). Here we analyze the optical characteristics of the NRD structure as it was indented to function in the fundamental quasi-TE mode (i.e.: as a NRD waveguide) with virtually all modes outside the core being cut off. We also consider its bending characteristics.

A recently proposed Metallo-Dielectric Waveguide (MDW) [38] provides long-range propagation at optical frequencies ($\sim 1.2dB/mm$) while allowing for aggressive bends ($r_0 \rightarrow 0$). Although these attributes are known to co-exist in some photonic crystal structures [39], the MDW offers the advantages of ease of fabrication and electrical contacts which could be used for optoelectronic/electro-optic functions.

In this paper we report a theoretical study of the parallel plate waveguide, the NRD waveguide and the MDW, at optical frequencies. The parallel plate waveguide is studied first in order to gain insight into the design and operation of the other two which both incorporate parallel plate sections. This is followed by a discussion of the NRD and MDW structures individually, showing the loss associated with various designs along with the ability of each structure to guide light around sharp radial bends, $r_0 \rightarrow 0$.

II. 1-Dimensional Analysis

A sketch of the parallel plate waveguide and of the main transverse electric field for numerous TE and TM parallel plate waveguide modes are shown in Fig. 1. The refractive index of the dielectric core and the metal are labeled n_D and n_m respectively with the parallel plates having a separation s. The field sketches are accurate for

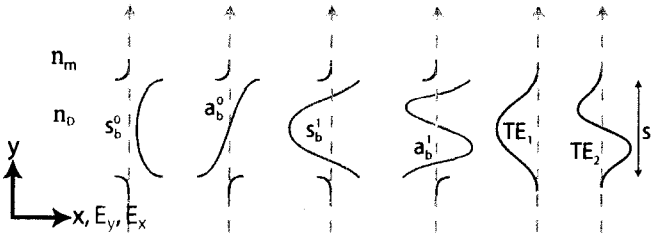

Fig. 1. Sketch of 1D parallel plate waveguide and of the first few modes supported therein. The main transverse electric field component is shown for the TM and TE modes by the blue and purple curves respectively. The dielectric core, with refractive index n_D, has a thickness s and metal claddings (n_m) above and below.

metals at optical frequencies ($\Re e\{\epsilon_{r,m}\} < 0$) which as a result causes the perpendicular electric field to change sign between the dielectric and metal regions, as observed in the E_y field of plasmonic TM modes. We analyze parallel plate waveguides along with a dielectric slab since they represent 1D cuts through sections of the NRD and MDW and will help better understand the guidance mechanism of these structures.

The waveguides were analyzed at a free space wavelength of λ_0=1550 nm. The metal plates were modelled as PECs and as a real metal. The effective index of the modes in the PEC case were calculated analytically using $n_{eff} = \sqrt{(2\pi n_D/\lambda_0)^2 - (m\pi/s)^2}/\beta_0$ [23] where m is the mode number, with $m = 0$ being the vertically polarized TEM mode and $m = 1, 2, 3...$ being the index of the degenerate TE_m and TM_m modes. The effective index of the single interface SPP, $n_{eff} = \sqrt{(n_D^2 * n_m^2)/(n_D^2 + n_m^2)}$ [24], is also computed for reference. The real metal parallel plate modes were calculated using the Transfer Matrix Method [40] with the metal plates being semi-infinite.

Fig. 2 shows the effect of the parallel plate waveguide's core thickness, s, on the effective index and mode power attenuation, which is given by $MPA = -0.02log_{10}(e)\beta_0\Im m(n_{eff})$ in dB/mm where $\beta_0 = 2\pi/\lambda_0$ is the free-space phase constant, in rad/m, and the free-space wavelength in vacuum; $e^{+j\omega t}$ time dependence implied. Au was chosen as the metal which has a relative permittivity of $\epsilon_{r,m} = -131.95 - 12.65i$ at λ_0=1550nm [41]. Between the plates is a dielectric core of index $n_D = 2.1375$, which is representative of Si_3N_4 and some electro-optic crystals such as $LiNbO_3$ and $PLZT$. We can see from Fig. 2 (a) that the TEM and s_b^0 modes remain guided as $s \to 0$. Both the TE_1 and a_b^0 mode have virtually the same cutoff thickness, s=321nm, while the degenerate TE_1 and TM_1 PEC modes, which appear to follow the same trend, have a slightly larger cutoff thickness ($s = \lambda_0/2n_D$) and a lower effective index. A similar observation can be made about the relation between the s_b^1 and TE_2 modes with respect to the TE_2 and TM_2 PEC modes. Fig. 2 (b) shows how the MPA changes as a function of s, where only the real metals are shown since there is no loss associated with the PEC modes (MPA = 0). The TM modes exhibit a higher loss than its paired TE mode, which is a result of the larger field penetration into the metal experienced by the TM modes.

To get of better understanding of the evolution of the real metal modes from the PEC modes we begin by

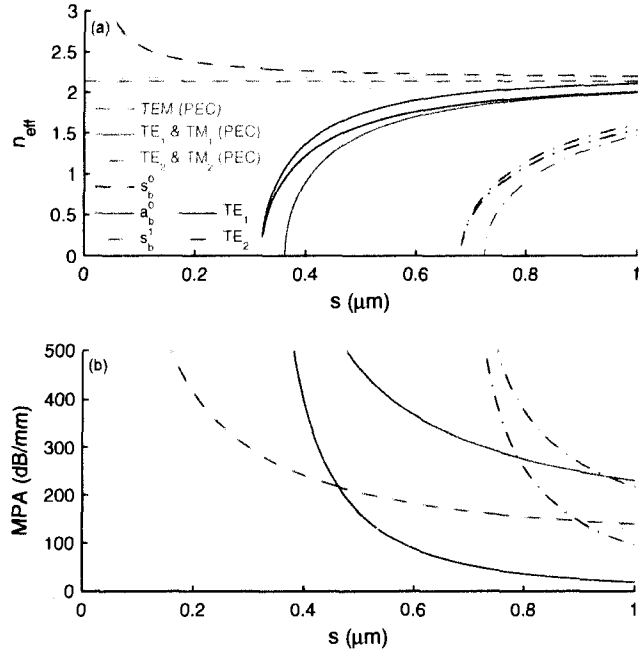

Fig. 2. (a) Effective index and (b) propagation loss of the modes as a function of changing thickness s for a parallel plate waveguide consisting of n_m-n_D-n_m, with $n_m = \sqrt{-131.95 - 12.65i}$ and $n_D = 2.1375$. The green curves show the modes of a parallel plate with PECs for the metal.

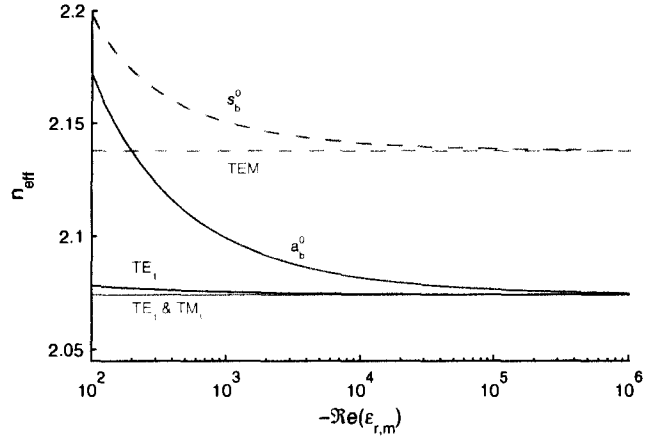

Fig. 3. Evolution of real metal (blue and purple) to PEC (green) parallel plate modes as $\Re e(\epsilon_{r,m}) \to -\infty$.

considering the Drude model which estimates the properties of a metal [42], [43]. The relative permittivity is given by $\epsilon_{r,m}(\omega) = 1 - \omega_p^2/(\omega^2 - i\omega/\tau)$ where $\omega_p = \sqrt{4\pi n e^2/m_e}$ is the plasma frequency with e, m_e and n being the electron charge, electron rest mass and number of electrons per cubic centimeter respectively. The electron density increases with conductivity implying that ω_p becomes ∞ for a PEC. The Drude model also assumes that there is a probability that electrons will experience a collision every τ seconds (or *unit time*), which becomes less

TABLE I
RELATION BETWEEN REAL METAL AND PEC PARALLEL PLATE MODES

real metal		PEC
s_b^0	$\rightleftharpoons$	TEM
a_b^0, TE_1	$\rightleftharpoons$	TM_1, TE_1
s_b^1, TE_2	$\rightleftharpoons$	TM_2, TE_2
a_b^1, TE_3	$\rightleftharpoons$	TM_3, TE_3
$\vdots$	$\rightleftharpoons$	$\vdots$

frequent in a good conductor, with $\tau = \infty$ for a PEC. Applying the PEC conditions yields $\Im m\{\epsilon_{r,m}\} \rightarrow 0$ and $\Re e\{\epsilon_{r,m}\} \rightarrow -\infty$. In Fig. 3 we show the evolution of the first three parallel plate modes as the relative permittivity changes from $\Re e\{\epsilon_{r,m}\}$=-100 (typical of Au/Ag at λ_0=1550 nm) to $\Re e\{\epsilon_{r,m}\} \rightarrow -\infty$. It shows the effective index of the s_b^0 mode converging to the TEM mode [26], [29], [30]. We also see the a_b^0 and TE_1 modes converge to the TE_1 and TM_1 PEC modes. Similar evolutions are noticed with the higher order modes, some of which are shown in Table I. Convergance of the TM modes occurs more slowly than its associated TE mode, which is no doubt a result of the larger field penetration in the metal for the TM modes.

In Fig. 4 (a) we again show the effective index of parallel plate modes and their dependence on s but for another dielectric core of index n_D=1.444. Trends remain similar to those made about Fig. 2, but cutoff thicknesses increase with, for example, the a_b^0 and TE_1 modes now cutting off at $s \sim 500nm$. The attenuation associated with these modes is lower for large s, however the propagation loss also begin to exponentially increase at larger separations.

Next we model a dielectric slab waveguide having an index profile n_2-n_1-n_2, where $n_1 = 2.1375$ and $n_2 = 1.444$, to show the dependence of the modes effective index on the core thickness s, see Fig. 5. Since the structure is symmetric both the TE_x and TM_x mode families have the same cutoff thickness with the fundamental TE and TM modes being supported to $s \rightarrow 0$. Single mode operation for either of the orthogonal TE_0 and TM_0 modes occurs for $s < 492nm$. These curves will be useful in the exploration of the NRD and MDW in the subsequent sections.

III. NON-RADIATIVE DIELECTRIC WAVEGUIDE

The NRD waveguide [32], shown in Fig. 6 in cylindrical co-ordinates, is made up of Au parallel plates of index n_m separated by s. A core, of width w and index $n_1 = 2.1375$, is bounded by low index material $n_2 = 1.444$ on either side. The structure supports families of quasi-TE and TM modes. The fundamental TE and TM modes are labeled E_{11}^{ρ} and E_{11}^{z} respectively, adopting the nomenclature introduced by Marcatili [44]. In the following analysis we are interested in the E_{11}^{ρ} mode only, which is commonly referred to as the LSM_{10} mode in microwave literature, due to it's low loss and non-radiative character. E_{11}^{ρ} evolves from the parallel plate TE_1 mode by introducing lateral

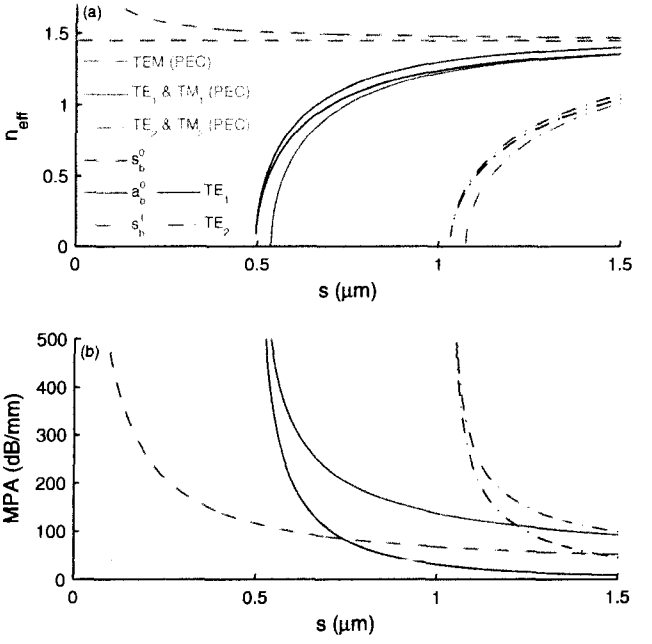

Fig. 4. (a) Effective index and (b) propagation loss of modes as a function of thickness s for a parallel plate waveguide consisting of n_m-n_D-n_m. The green curves show the modes of a parallel plate with PECs, with $n_m = \sqrt{-131.95 - 12.65i}$ and $n_D = 1.444$

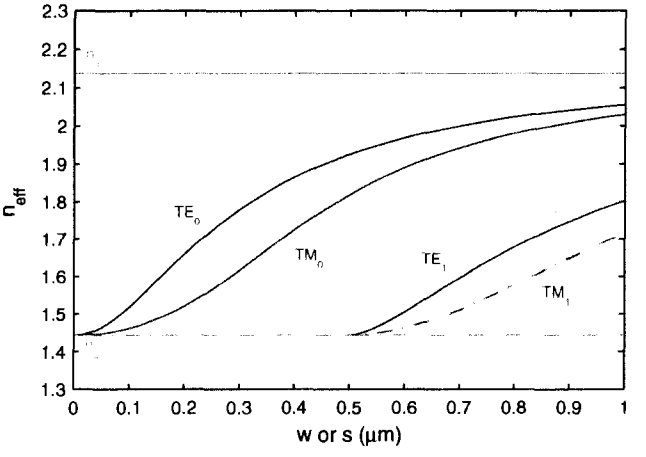

Fig. 5. Effective index of dielectric slab waveguide modes, n_2-n_1-n_2, as a function of core thickness.

confinement which, in this case, is achieved placing lower index material next to the core and suppressing all modes in this region. A NRD waveguide with PECs requires a thickness $s < \lambda_0/2n_2$ while a numerical solution can be employed for the Au parallel plates at optical frequencies, as shown in Fig.4 (a) with the cutoff of the a_b^0 and TE_1 being $s \sim 500nm$. We choose the core thickness to be $s = 500nm$ because it offers the lowest attenuation based on the materials used. NRD designs at microwave frequencies often have a dielectric core with air on either

side, rather than a dielectric material. This is not easily conceivable at optical frequencies since it seems difficult to fabricate. COMSOL [45] was used to model the straight waveguides, $r_0 = \infty$, and the method of lines [9] for bent structures, since both tools provide full wave electromagnetic modeling. The cylindrical coordinate system will be used subsequently for all 2D structures with waveguide propagating along the + ϕ-axis and following a $e^{-j\beta_o\phi} = e^{jn_{eff}\beta_0 r_0\phi}$ dependency.

A. *Straight Waveguide Analysis*

Modal analysis is performed on two NRD waveguides both having a separation of $s = 500nm$. The influence of the waveguide width on the effective index of the first two fundamental quasi-TE modes, E_{11}^{ρ} and E_{21}^{ρ} at $r_0 = \infty$, is shown in Fig. 7. One of the waveguides is modeled with real metal properties and the other with PECs shown by the black and green curves respectively. Insets to Fig. 7 (b) show E_ρ and E_z field components of the E_{11}^{ρ} mode at various widths.

From Fig. 7 (a) it is noticed that the cutoff of the PEC modes is abrupt when compared to the real metal modes. Below the cutoff width of the PEC modes there is a significant drop in the effective index of the real metal modes. This same region also shows a sharp increase in the mode's propagation loss, see Fig. 7 (b). Examination of the fields in this region for the real metal case shows a transformation of their dominant TE character toward the asymmetrically coupled surface plasmons between the upper and lower surface. The field distributions are similar to the a_b^0 parallel plate mode which explains the increased propagation loss since at $s = 500nm$ the mode has an attenuation value that is several orders of magnitude higher than the TE_1 mode at $s = 500nm$, see Fig.2 (b).

When looking at the MPA for larger waveguide widths it is noticed that the loss reaches a minimum of ~165 dB/mm. Comparing this to the computed propagation loss in Fig. 2 of the TE_1 parallel plate mode we can see that the loss at s=500nm is virtually the same as the NRD waveguide at large w. Results show that our NRD waveguide exhibits losses that are too high for most practical use; one way to reduce the propagation loss without changing the core material is to increase s, while still retaining its non-radiative ability. This could be achieved by using a lower refractive index material, for the claddings (n_2), hence increasing the cutoff width of the modes outside the core and allowing for a larger s. If single mode operation is required then a minimum loss of ~60dB/mm (at $s = 683$) could be reached for a waveguide with core n_1, as shown in Fig. 2 (b).

There are features in the MPA curves, especially for the E_{11}^{ρ} mode near $w \sim 4\mu m$ and $w \sim 6\mu m$, seen in Fig. 7 (b). Similar to the rectangular dielectric waveguide the fundamental quasi-TE mode of the NRD has an E_z field component. The complication with the NRD waveguide is that the E_z field exists at the corners of the core, similar to the rectangular dielectric waveguide, only now (at optical wavelengths) the metal interfaces support surface plasmons. Since adjacent corners have E_z fields of opposite sign, asymmetric SPPs become coupled to the

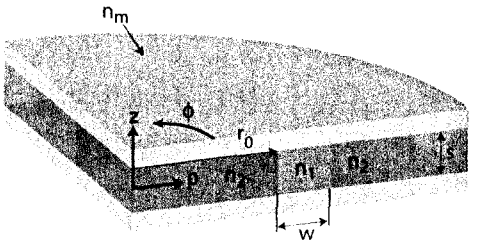

Fig. 6. NRD waveguide shown in cylindrical co-ordinates.

quasi-TE mode. Three pairs of field contour plots are shown for various waveguide widths, with the E_ρ field shown on top and E_z on the bottom. One can see how the field is evolving across the feature located $w \sim 4\mu m$. Notice that there is always an even number of E_z field peaks along the metal surface since it is necessary to maintain adjacent E_z fields of opposite sign as dictated by the symmetry of the E_{11}^ρ mode. As the waveguide becomes wider pairs of additional positive and negative E_z field peaks become allowed. When this occurs there is a transition where little to no E_z field exists at the corners and the mode begins to looses its TE character, as seen by the inset at $w = 3.98\mu m$ resulting in a higher loss.

B. Bent Waveguide Analysis

The simulated bending results, shown in Fig. 8, give the insertion loss through a 90^0 bend along with the effective index of the E_{11}^ρ mode for an NRD waveguide with $w = 2.2\mu m$ and $s = 500nm$. The width was chosen to support single mode operation. The E_{21}^ρ mode is still slightly guided but is highly perturbed at this width due to strong coupling to SPPs and is thus expected to have a low excitation efficiency and to attenuate quickly. Even though the s_b^0 mode is supported to zero thickness the NRD waveguide is able to effectively suppress radiation, due to orthogonality. In Fig. 8 (a) the insertion loss with changing radius of curvature, r_0 shows a trend that is different from that of radiative lossy waveguides [9] whereby the IL normally decreases with r_0 until the waveguide begins to radiate. In that situation the overall IL is dominated by propagation loss for large r_0 then as r_0 becomes small the dominant loss mechanism shifts to radiation, resulting in an optimum radius of curvature, $r_{0,opt}$ [9]. Since the NRD never actually radiates the loss continues to decrease with the radius. The shape of the mode does however show dramatic changes as $r_0 \to 0$, losing its dominant TE character. This change can be seen from the field contours of the S_ϕ component of the Poynting vector, shown as insets. For large r_0 the TE character is predominant, as seen by S_ϕ at $r_0 = 45\mu m$, while the other two insets show that for $r_0 < 15\mu m$ more power is transfered to the SPPs on the upper and lower surface.

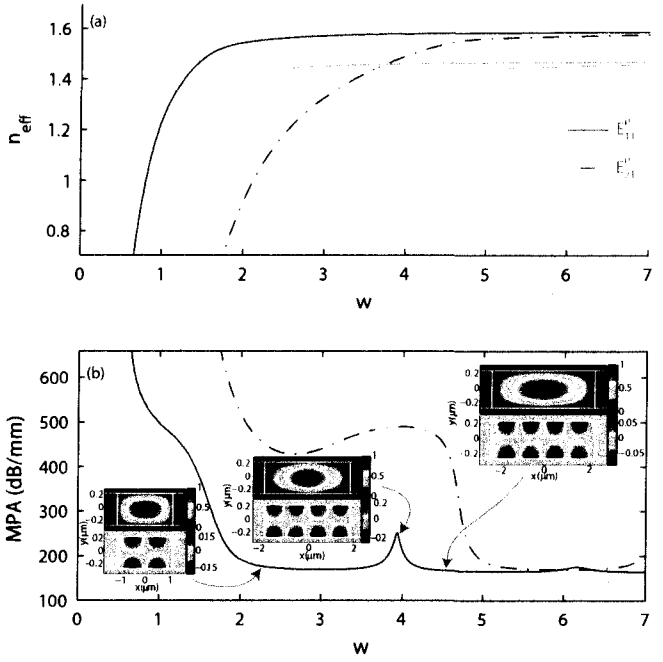

Fig. 7. (a) Effective index and (b) propagation loss of the E_{11}^{ρ} and E_{21}^{ρ} modes as a function of core width for the straight ($r_0 = \infty$) NRD waveguide. Insets show the mode fields at $w = 2.2, 3.98$ and $4.5\mu m$, with the E_ρ field component on top and E_z on the bottom.

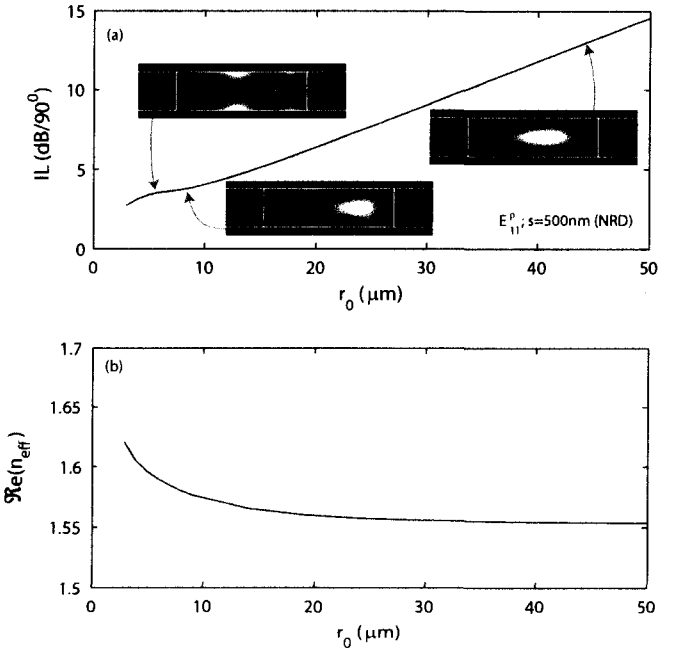

Fig. 8. (a) insertion loss through a 90^0 bend and (b) effective index as a function of the radius of curvature for a single mode NRD waveguide (s=500nm, w=2.2μm). Insets show the S_ϕ component of the pointing vector for r_0=5, 8 and $45\mu m$.

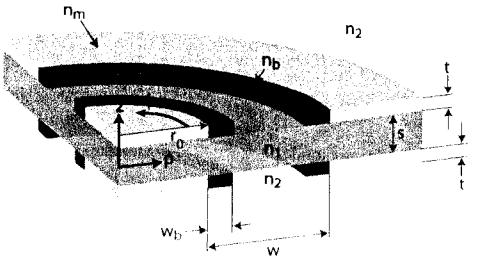

Fig. 9. MDW design shown in cylindrical co-ordinates.

IV. Metallo-Dielectric Waveguide

In this section we describe some design possibilities for the MDW, which is shown in Fig. 9 in cylindrical co-ordinates [38]. The waveguide consists of a dielectric core, $n_1 = 2.1375$, of thickness s and a dielectric cladding, $n_2 = 1.444$, providing the vertical confinement through a step in index ($n_2 < n_1$). Au Parallel plates of thickness t and index n_m are located on either side of the core providing the mode with lateral confinement. High index $n_b = 3.4757$ dielectric plugs of width w_b, were found to reduce the overall propagation loss when placed at the edge of the metal. The lateral confinement imposed by this structure is similar in nature to a step in refractive index only with confinement being assessed with respect to modes in the parallel plate waveguide rather than plane waves. The fundamental mode of the MDW evolves from the TE_0 dielectric slab mode which has an effective index, Fig.5, that remains above those of the TE and TM modes in the parallel plate waveguide, with $n_D = 2.1375$ seen in Fig.2 (a), creating a form of confinement. Although the index of the s_b^0 mode is above the TE_0 mode essentially no coupling is expected due to orthogonality. Confinement is expected for any core thicknesses; however, if we bring this thickness below the cutoff of the parallel plate modes (ie.: $s \leq 300nm$) the bending capabilities of the waveguide could be greatly improved since essentially all radiation channels are suppressed, similar to the NRD waveguide.

A. Straight Waveguide Analysis

Fig. 10 shows the dispersion of the E_{11}^{ρ} and E_{21}^{ρ} modes with $r_0 = \infty$ as a function of the waveguide width. A metal thickness of $t = 200nm$ and a plug width of $w_b = 0.2\mu m$ were used. Two core thicknesses are considered; one with $s = 300nm$, where the parallel plate modes are cut off, and another with $s = 500nm$, where the a_b^0 and s_b^1 parallel plate waveguide modes are guided. The propagation loss drastically increases as the cutoff width is approached, due to the mode fields closer proximity to the metal. The thicker waveguide has a lower attenuation than the thinner one, although it lacks the non-radiative character as discussed further below. The inset in Fig. 10 (b) shows the low loss region of the waveguide, with propagation losses of $\sim$ 2.37 dB/mm being achievable. If the width is increased even more, to $w = 5\mu m$, the even lower losses of $\sim$ 1.2 dB/mm are reported [38]. The low

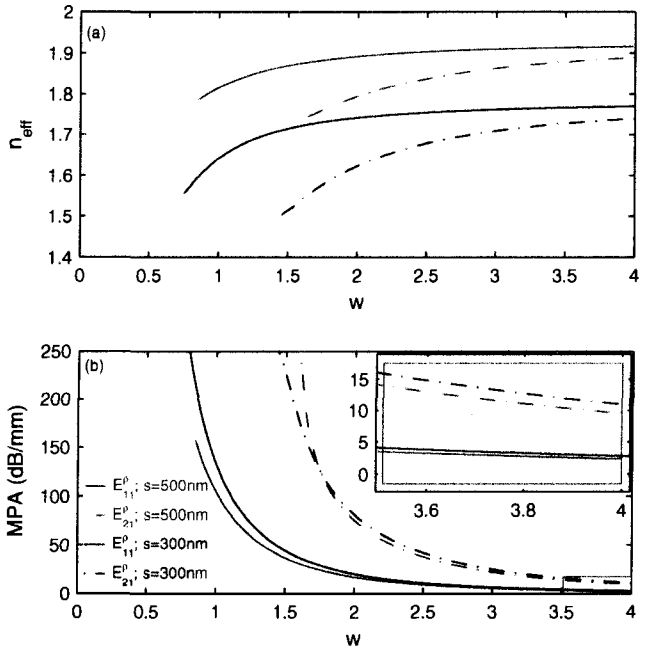

Fig. 10. (a) Effective index and (b) propagation loss of the E_{11}^{ρ} mode as a function of the core width, w, for the straight ($r_0 = \infty$) MDW. Two design thicknesses, $s = 300nm$ and $s = 500nm$, are considered, both with $w_b = 0.2\mu m$ and $t = 200$.

radiation character, discussed later, renders the advantage of allowing short tapers for quick transitions between wider low loss and narrow single mode sections.

Fig.11 shows the dependence of the E_{11}^{ρ} modes' (a) effective index and (b) propagation loss on the plug width, w_b. Two waveguide widths, $w = 1.7\mu m$ and $w = 4\mu m$, and two thicknesses, $s = 300nm$ and $s = 500nm$, are considered. The high index dielectric plugs (n_b) have a dramatic effect on the attenuation of the fundamental mode and when dimensioned properly the plugs are able to lower the propagation loss by more than an order of magnitude, as shown in Fig. 11 (b). In the low loss region the dielectric plugs aid in repelling the fields away from the metal. When the plug becomes too narrow the E_{11}^{ρ} mode experiences direct contact with the with the metal causing higher excitation of SPPs. At the other extreme, when the the plugs become too large they are independently able to support their own guided modes. In this situation fields become confined within the plugs themselves causing higher field concentration to the edge of the metal. This is attributed to the increase in both the loss and effective index for $w_b > 0.25\mu m$. 1D analysis of a slab consisting of $n_m - n_b - n_1$ (i.e. horizontal cut along the plug) verifies the existence of this TM_1 plug mode which has a cutoff of $w_b = 0.22\mu m$. The loss of this 1D mode drastically increases to ~245dB/mm for w_b=0.3 μm, however the plug mode supported by the MDW is significantly less confined than the 1D mode due to the finite thickness.

Insets are used to illustrate the effect of the plug by showing the E_ρ field component for $w_b = 0.020$, 0.2 and

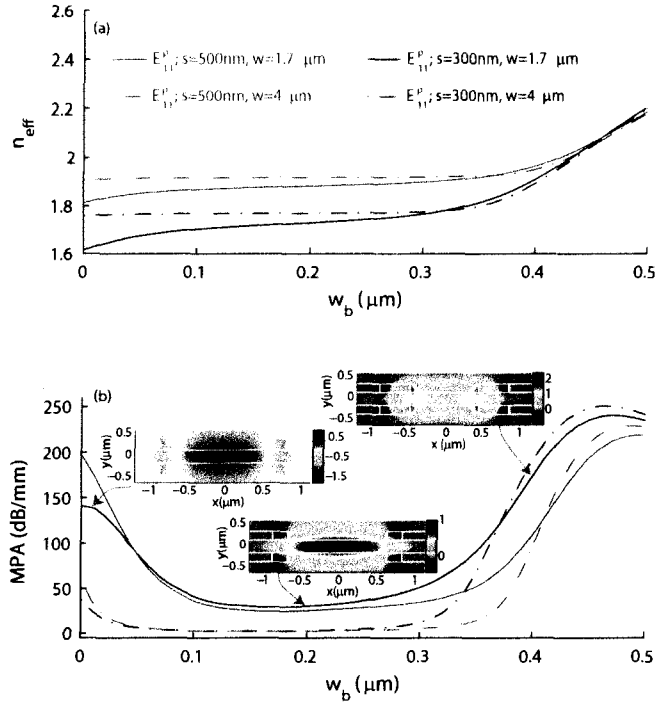

Fig. 11. (a) Effective index and (b) propagation loss of the E^{ρ}_{11} and E^{ρ}_{21} modes as a function of plug width, w_b, for the straight ($r_0 = \infty$) MDW. Two design thicknesses, $s = 300nm$ and $s = 500nm$, are considered, with $t = 200nm$ and $w = 1.7\mu m$. The E_x field component is shown in inset for select plug widths (w_b = 20, 200 and 400nm) of the s =300nm t =200nm w =1.7μm waveguide.

$0.4\mu m$. The E_ρ field associated with the design having large plugs looks like four coupled plug modes rather than a single TE mode. The E_ρ fields of the other two modes have an apparent single TE mode character in the center of the waveguide with the $w_b = 0.2\mu m$ waveguide showing a minimized fields localized at the edge of the metal.

B. Bent Waveguide Analysis

Simulated bending results are shown in Fig. 12 for a number of MDW designs along with a comparable, high confinement, single mode dielectric waveguide for comparison. The dielectric waveguide has a thickness $s = 300nm$ and width $w = 800nm$, with a core and cladding index of n_1 and n_2 respectively. The best performance is seen by the MDW design with $s = 300nm$ and $t = 100nm$ which produces even better bending characteristics than the rectangular dielectric waveguide at small r_0. The design is capable of producing a calculated insertion loss of only 0.61dB/mm at $r_0 = 150nm$. Numerical limitations restricted r_0 from reaching zero but it is expected that the IL will continue to decrease as $r_0 \to 0$, as the trend suggests. At tight radii this mode has a small amount of leakage into single interface SPPs on the upper and lower surfaces of the metal plates [38]. Fig. 12 (a) and (e) shows that there are regions where the IL and n_{eff} curves are not smooth with changing r_0. A magnification of these regions is shown in Fig. 12 (b), (c) and (d). Inspection of the fields shows that there is a resonance occurring where the

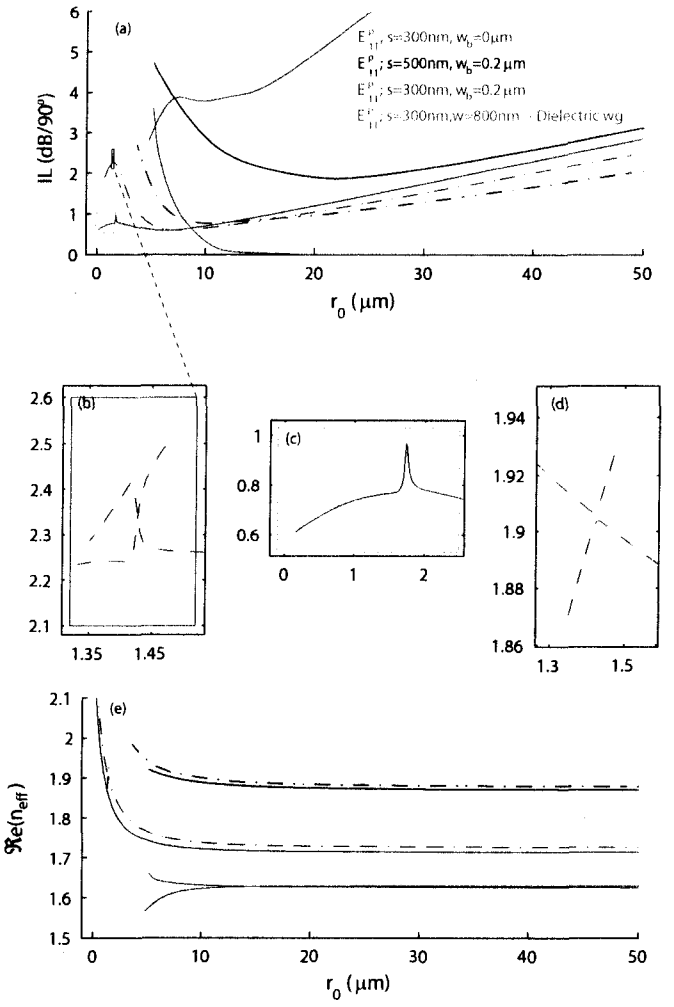

Fig. 12. (a) Insertion loss through a 90^0 bend and (e) effective index as a function of the radius of curvature for various MDW designs along with a single mode dielectric waveguide. Structures with t=100nm and t=200nm are represented by the line style '—' and by '–.–' respectively.

optical energy is transferred to the dielectric plugs. In the case of $t = 200$ there are actually two separate modes that exist, one becoming cut off as r_0 increases and the other as r_0 decreases, see Fig. 12 (d). The fundamental TE character remains the same for both these modes away from cutoff but there is a slight difference in the fields inside the plug.

The importance of the plugs is illustrated by the MDW with $w_b = 0$. As mentioned before this straight waveguide ($r_0 = \infty$) has strong field localization at the edge of the metal. This is only made worse as r_0 decreases. Observation of the mode fields reveals radiation into single interface SPP is near $r_0 = 20\mu m$. At approximately $r_0 = 9\mu m$ the IL begins to decrease again and through evaluation of the fields it was noticed that there is a large field concentration along the inner metal edges, which form asymmetrically coupled corner SPPs between the upper and lower metal

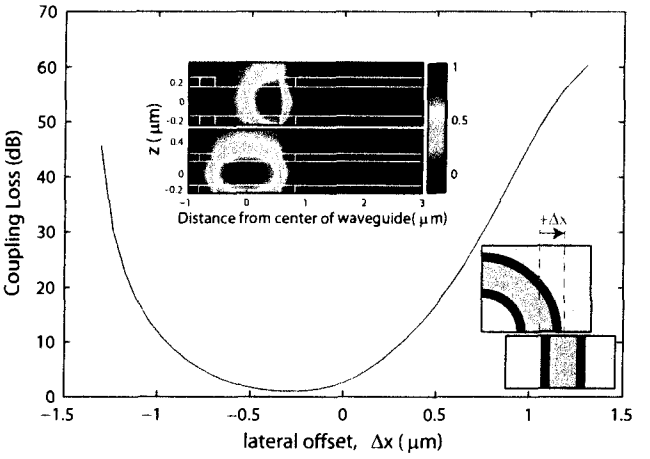

Fig. 13. Coupling loss between a straight (r_0=∞) and bent (r_0=0.4μm) MDW as a function of the lateral offset Δx. Both waveguides are dimensioned with w=1.7μm, w_b=0.2μm, s=300nm, t=100nm. The inset is a top view of the straight and bend waveguide illustrating the $\pm$ offset.

plate. This phenomenon is believed to be the cause of the decrease in n_{eff} observed Fig. 12 (e), based on the fact that the coupled corner modes have fields that resemble the a_b^0 slab mode, which has subwavelength characteristics near cutoff. Two MDW designs with a thicker core, one with $t = 100nm$ and the other $t = 200nm$, are also shown. Both of these designs support a guided mode as r_0 decreases and show less radiation than expected, despite coupling into the a_b^0 and s_b^1 modes of the parallel plate at the outer edge. Field plots can be seen in Fig. (d) and (e) from [38] of the E_{11}^{ρ} mode, for the waveguide dimensioned $w = 1.7\mu m$ $s = 300nm$ and $t = 100nm$ at $r_0 = 5.15\mu m$, clearly radiating into the a_b^0 and s_b^1 modes.

Finally since there is usually deformation of the bent waveguide modes an estimate of the coupling loss is calculated by computing the overlap integral between the main TE field component, $E\rho$, of the straight $r_0 = \infty$ and bent $r_0 = 0.4\mu m$ waveguide, designed with $w = 1.7\mu m$, $s = 300nm$, $w_b = 0.2\mu m$ and $t = 100nm$. Fig.13 shows the coupling loss as a function of the lateral offset Δx, with the bottom-right inset showing the two waveguides in top view illustrating the positive and negative offset. The inset in the center of the figure shows the E_ρ field component of both the bent (top) and straight (bottom) waveguides. Results show that a slight offset of $\Delta x \sim -300nm$ reduces the transitin loss to <1dB as compared to 3.6dB with no offset.

V. Conclusion

In summary, we have modeled and shown the theoretical bending characteristics of both the NRD and MDW. From the 1D analysis, which was primarily used as an aid in the 2D waveguide design, we were able to show the relation between the modes that exist in a parallel plate waveguide with real metal and PEC, at optical frequencies.

The analysis of the NRD waveguide showed that although the structure is able to support a non-radiative and low

loss mode at microwave frequencies, these properties are not carried over at optical wavelengths; The waveguide exhibits high losses of $\sim$ 165 dB/mm and experiences significant field deformation when bent aggressively.

Encouraging results are obtained for the MDW. We were able to show that long-range propagation, $\sim 1.2dB/mm$, is possible through careful dimensioning of the dielectric plugs and waveguide width. The E_{11}^{ρ} mode is also able to undergo low loss 90^0 radial bends as $r_0 \rightarrow 0$, while retaining its fundamental TE character. These attributes along with the possibility for optoelectronic/electro-optic functions make this structure interesting and worth further investigation.

REFERENCES

[1] R. L. Espinola, R. U. Ahmad, F. Pizzuto, M. J. Steel, and R. M. Osgood, "A study of high-index-contrast 90 degrees waveguide bend structures," *Opt. Express*, vol. 8, no. 9, pp. 517–528, 2001.

[2] M. Popovic, K. Wada, S. Akiyama, H. A. Haus, and J. Michel, "Air trenches for sharp silica waveguide bends," *J. Lightwave Technol.*, vol. 20, no. 9, pp. 1762–72, 2002.

[3] B. M. A. Rahman, D. M. H. Leung, S. S. A. Obayya, and K. T. V. Grattan, "Numerical analysis of bent waveguides: bending loss, transmission loss, mode coupling, and polarization coupling," *Appl. Optics*, vol. 47, no. 16, pp. 2961–2970, 2008.

[4] A. Sakai, G. Hara, and T. Baba, "Propagation characteristics of ultrahigh-delta optical waveguide on silicon-on-insulator substrate," *Jpn. J. Appl. Phys. 2*, vol. 40, no. 4B, pp. L383–L385, 2001.

[5] Y. A. Vlasov and S. J. McNab, "Losses in single-mode silicon-on-insulator strip waveguides and bends," *Opt. Express*, vol. 12, no. 8, pp. 1622–1631, 2004.

[6] P. Berini, "Figures of merit for surface plasmon waveguides," *Opt. Express*, vol. 14, no. 26, pp. 13 030–13 042, 2006.

[7] ——, "Long-range surface plasmon-polariton waveguides in silica," *J. Appl. Phys.*, vol. 102, no. 5, pp. 053 105–1–8, 2007.

[8] ——, "Plasmon-polariton waves guided by thin lossy metal films of finite width: Bound modes of symmetric structures," *Phys. Rev. B*, vol. 61, no. 15, pp. 10 484–10 503, 2000.

[9] P. Berini and J. Lu, "Curved long-range surface plasmon-polariton waveguides," *Optics Express*, vol. 14, no. 6, pp. 2365–2371, 2006.

[10] P. Berini, "Plasmon-polariton modes guided by a metal film of finite width bounded by different dielectrics," *Optics Express*, vol. 7, no. 10, pp. 329–335, 2000.

[11] R. Charbonneau, C. Scales, I. Breukelaar, S. Fafard, N. Lahoud, G. Mattiussi, and P. Berini, "Passive integrated optics elements used on long-range surface plasmon polaritons," *Journal of Lightwave Technology*, vol. 24, no. 1, pp. 477–494, 2006.

[12] S. Jette-Charbonneau, R. Charbonneau, N. Lahoud, G. Mattiussi, and P. Berini, "Demonstration of bragg gratings based on long-ranging surface plasmon polariton waveguides," *Optics Express*, vol. 13, no. 12, pp. 4674–4682, 2005.

[13] A. Degiron and D. R. Smith, "Numerical simulations of long-range plasmons," *Optics Express*, vol. 14, no. 4, pp. 1611–1625, 2006.

[14] A. Degiron, C. Dellagiacoma, J. G. McIlhargey, G. Shvets, O. J. F. Martin, and D. R. Smith, "Simulations of hybrid long-range plasmon modes with application to 90 degrees bends," *Optics Letters*, vol. 32, no. 16, pp. 2354–2356, 2007.

[15] A. Degiron, S. Y. Cho, C. Harrison, N. M. Jokerst, C. Dellagiacoma, O. J. F. Martin, and D. R. Smith, "Experimental comparison between conventional and hybrid long-range surface plasmon waveguide bends," *Phys. Rev. A*, vol. 77, no. 2, pp. 021 804–1–4, 2008.

[16] A. Boltasseva, T. Nikolajsen, K. Leosson, K. Kjaer, M. S. Larsen, and S. I. Bozhevolnyi, "Integrated optical components utilizing long-range surface plasmon polaritons," *J. Lightwave Technol.*, vol. 23, no. 1, pp. 413–422, 2005.

[17] D. F. P. Pile and D. K. Gramotnev, "Channel plasmon-polariton in a triangular groove on a metal surface," *Opt. Lett.*, vol. 29, no. 10, pp. 1069–1071, 2004.

[18] S. I. Bozhevolnyi, "Effective-index modeling of channel plasmon polaritons," *Opt. Express*, vol. 14, no. 20, pp. 9467–9476, 2006.

[19] S. I. Bozhevolnyi, V. S. Volkov, E. Devaux, J. Y. Laluet, and T. W. Ebbesen, "Channel plasmon subwavelength waveguide components including interferometers and ring resonators," *Nature*, vol. 440, no. 7083, pp. 508–511, 2006.

[20] V. S. Volkov, S. I. Bozhevolnyi, E. Devaux, and T. W. Ebbesen, "Bend loss for channel plasmon polaritons," *Appl. Phys. Lett.*, vol. 89, no. 14, pp. 143 108–1–3, 2006.

[21] B. Steinberger, A. Hohenau, H. Ditlbacher, A. L. Stepanov, A. Drezet, F. R. Aussenegg, A. Leitner, and J. R. Krenn, "Dielectric stripes on gold as surface plasmon waveguides," *Appl. Phys. Lett.*, vol. 88, no. 9, pp. 94 104–1–3, 2006.

[22] A. V. Krasavin and A. V. Zayats, "Passive photonic elements based on dielectric-loaded surface plasmon polariton waveguides," *Appl. Phys. Lett.*, vol. 90, no. 21, pp. 211 101–1–3, 2007.

[23] D. K. Cheng, *Field and Wave Electromagnetics*, 2nd ed. New York: Addison-Wesley, 1989.

[24] H. Raether, *Surface Plasmons on Smooth and Rough Surfaces and on Gratings*, ser. Springer Tracts in Modern Physics. New York: Springer-Verlag, 1988, vol. 111.

[25] K. Ki Young, C. Young Ki, T. Heung-Sik, and L. Jeong-Hae, "Light transmission along dispersive plasmonic gap and its subwavelength guidance characteristics," *Optics Express*, vol. 14, no. 1, pp. 320–329, 2006.

[26] R. Gordon, "Light in a subwavelength slit in a metal: propagation and reflection," *Physical Review B (Condensed Matter and Materials Physics)*, vol. 73, no. 15, pp. 153 405–1, 2006.

[27] G. Veronis and S. H. Fan, "Bends and splitters in metal-dielectric-metal subwavelength plasmonic waveguides," *Applied Physics Letters*, vol. 87, no. 13, p. 3, 2005.

[28] ——, "Modes of subwavelength plasmonic slot waveguides," *Journal of Lightwave Technology*, vol. 25, no. 9, pp. 2511–2521, 2007.

[29] E. Feigenbaum and M. Orenstein, "Modeling of complementary (void) plasmon waveguiding," *Journal of Lightwave Technology*, vol. 25, no. 9, pp. 2547–62, 2007.

[30] J. A. Dionne, L. A. Sweatlock, H. A. Atwater, and A. Polman, "Plasmon slot waveguides: towards chip-scale propagation with subwavelength-scale localization," *Physical Review B (Condensed Matter and Materials Physics)*, vol. 73, no. 3, pp. 35 407–1, 2006.

[31] R. Zia, M. D. Selker, P. B. Catrysse, and M. L. Brongersma, "Geometries and materials for subwavelength surface plasmon modes," *Journal of the Optical Society of America A: Optics and Image Science, and Vision*, vol. 21, no. 12, pp. 2442–2446, 2004.

[32] T. Yoneyama and S. Nishida, "Nonradiative dielectric waveguide for millimeter-wave integrated-circuits," *IEEE T. Micro. Theory*, vol. 29, no. 11, pp. 1188–1192, 1981.

[33] ——, "Nonradiative dielectric waveguide circuit components," *Int. J. Infrared Milli.*, vol. 4, no. 3, pp. 439–449, 1983.

[34] T. Yoneyama, "Nonradiative dielectric waveguide," in *Infrared and millimeter waves. Vol.11. Millimeter components and techniques, part III*. Academic Press, 1984, pp. 61–98.

[35] T. Yoneyama, H. Sawada, and T. Shimizu, "Nrd-guide passive components and devices for millimeter wave wireless applications," *IEICE T. Electron.*, vol. E90C, no. 12, pp. 2170–2177, 2007.

[36] F. Kusunoki, T. Yotsuya, J. Takahara, and T. Kobayashi, "Propagation properties of guided waves in index-guided two-dimensional optical waveguides," *Applied Physics Letters*, vol. 86, no. 21, pp. 211 101–1–3, 2005.

[37] F. Kusunoki, T. Yotsuya, and J. Takahara, "Confinement and guiding of two-dimensional optical waves by low-refractive-index cores," *Optics Express*, vol. 14, no. 12, pp. 5651–5656, 2006.

[38] R. Buckley and P. Berini, "Long-range substantially nonradiative metallo-dielectric waveguide," *Optics Letters*, 2008, submitted.

[39] A. Mekis, J. C. Chen, I. Kurland, S. Fan, P. R. Villeneuve, and J. D. Joannopoulos, "High transmission through sharp bends in photonic crystal waveguides," *Phys. Rev. Lett.*, vol. 77, no. 18, pp. 3787–90, 1996.

[40] C. K. Chen, P. Berini, D. Z. Feng, S. Tanev, and V. P. Tzolov, "Efficient and accurate numerical analysis of multilayer planar optical waveguides in lossy anisotropic media," *Opt. Express*, vol. 7, no. 8, pp. 260–272, 2000.

[41] E. Palik, *Handbook of Optical Constants of Solids*. New York: Academic Press, 1985.

[42] I. Mermin and N. D. Mermin, *Solid State Physics*. Toronto: Thomsom Learning, 1976.

[43] W. L. Barnes, "Surface plasmon-polariton length scales: a route to sub-wavelength optics," *Journal of Optics a-Pure and Applied Optics*, vol. 8, no. 4, pp. S87–S93, 2006.

[44] E. A. J. Marcatili, "Dielectric rectangular waveguide and directional coupler for integrated optics," *Bell Tech. J.*, vol. 48, no. 7, pp. 2071–102, 1969.

[45] COMSOL, *Electromagnetic Module*, 2005, v3.2.

Chapter 5

Conclusion

5.1 Thesis contributions

Variations of the plasmonic metal stripe were analyzed and compared based on figures of merit. Results show that even for 2D plasmonic waveguides there is a strong link between attenuation and confinement, whereby one is limited to a waveguide with either low loss and low confinement or with high loss and high confinement. Through analysis of gold, silver and aluminum stripes over a wavelength range about the visible spectrum optimum wavelengths of operation were found for each of the metals, with aluminum performing better below visible, silver possibly being better in the visible through to the infrared and gold showing slightly better performance over silver further into the infrared spectrum.

The parallel plate analysis, which was primarily used as an aid in the 2D waveguide design, revealed the relation between the modes supported by the real metal and perfect electric conductors (PECs) through manipulation of the Drude model to see how the metal properties change as the material becomes more like a PEC.

The NRD waveguide has the ability to suppress radiation; however, when operating at optical wavelengths the fundamental mode experiences large propagation loss due to the excitation of SPPs. These plasmons also cause the mode to become highly deformed, and essentially unusable, when bent aggressively. Many of the key features that the waveguide has at microwave frequencies appear to be lost when rescaled for

optical use.

The newly introduced MDW, on the other hand, has the ability to suppress radiation through aggressive bends, as $r_0 \rightarrow 0$, while maintaining it's fundamental TE character. Low loss propagation can be achieved by flaring the waveguide out to a larger width. The metal contacts also make the waveguide a candidate for use in optoelectronic/electro-optical devices.

5.2 Suggestions for future work

Although rigorous simulations have been performed on the MDW their performance has not been experimentally verified as of yet. It would seem logical to next have the waveguides manufactured for testing. It would be interesting use electro-optic crystals when building the waveguides in order to test the electro-optic abilities as well.

One could also foresee additional simulation work in order to optimize either of the NRD or MDW waveguides. Since both waveguides have many parameters there is a large design space that needs to be looked at.

Appendix A

On the convergence and accuracy of mode computations of surface plasmon waveguides

My contribution: For this paper I supplied convergence results based on COMSOL simulations, along with bent waveguide results using the method of lines, and created the figures from my results. Other results were generated by Dr. Berini and the paper was written by him. This paper has been accepted for publication in the Journal of Computational and Theoretical Nanoscience.

On the convergence and accuracy of mode computations of surface plasmon waveguides

Pierre Berini[1]

School of Information Technology and Engineering, University of Ottawa, 161 Louis Pasteur St., Ottawa, ON, K1N 6N5, Canada, and Spectalis Corp., P.O. Box 72029, Kanata North RPO, Ottawa, ON, K2K 2P4, Canada

Robin Buckley

School of Information Technology and Engineering, University of Ottawa, 161 Louis Pasteur St., Ottawa, ON, K1N 6N5, Canada

Keywords: surface, plasmon, waveguides, numerical, modelling, convergence, accuracy

Abstract

Two-dimensional surface plasmon-polariton waveguides must generally be analysed using numerical methods. However, accurate analysis is challenging due to large permittivity contrasts and to strong localisation of mode fields, especially near corners where they tend to diverge. These difficulties impact the convergence of numerical methods, yet understanding convergence is essential if accuracy is to be claimed. The convergence and accuracy of two vectorial numerical methods commonly used, the method of lines and the finite element method, were assessed by computing the propagation constant of modes supported by the metal slab, the metal stripe and the 90° metal corner. A discretisation strategy that yields smooth monotonic convergence is demonstrated for both methods. More accurate results are then extrapolated from the convergence histories and anticipated errors (relative to extrapolated results) are computed. Both methods yield similar anticipated errors for a comparable discretisation spacing, with the finite element method yielding slightly lower errors but the method of lines requiring less computational effort. Convergence was slower for highly confined modes, particularly those having fields localised near corners. Convergence to within an anticipated error of ±2% was readily achieved with both methods, except for the attenuation of modes that are highly localised to corners which remained in error by 10 to 20%. However, the percentage difference between the extrapolated results computed from both methods ranged from 3.75 to 0.012%. The convergence and accuracy of the methods of lines for curves was also investigated, and it was found that the absorbing boundary condition used along the radiating side of the curve introduces errors that can further limit the accuracy of the computations.

[1]Corresponding author: Fax (613) 562-5175, berini@site.uottawa.ca

1. Introduction

The surface plasmon-polariton (SPP)[1] is a TM-polarised surface wave propagating typically, but not exclusively, along the interface between optically semi-infinite metal and dielectric regions at optical wavelengths. This simple waveguide structure, henceforth referred to as the "single-interface", provides 1D field confinement in the direction perpendicular to the interface, with mode fields peaking at the interface and decaying exponentially away, and propagation occurring in the plane of the interface. Confinement (non-radiative, purely bound) of the SPP to the interface depends on having different signs for the real part of the permittivity of the media on either side. For dielectrics, the real part of permittivity is normally positive (away from resonances), and for most metals, the real part of permittivity is normally negative (below the plasma frequency).

Various SPP-supporting structures based on metal films, stripes, particles, or other geometries such as apertures in metal films, have been studied over time[2,3], exhibiting interesting and potentially useful properties, such as a high surface sensitivity, sharp resonances, strong dispersion, sub-wavelength confinement, and transmission through sub-wavelength apertures. SPP waveguides represent an important subset of such structures, generally constituted of a structured or patterned metal layer(s) bounded by dielectric(s), often comprising optically-coupled metal-dielectric interfaces and/or metal corners. Given that a single metal-dielectric interface supports an SPP, then even the simplest structures, such as a thin metal stripe, have a rich mode spectrum that can evolve in a complex manner with geometrical parameters, materials, and operating wavelength.

1D SPP waveguides, described by only one transverse dimension, and consisting of piece-wise continuous metal and dielectric regions, can be analysed analytically, in the sense that their cross-sectional domain not need be discretised. The SPP of the single-interface, for instance, is described mathematically in closed form[1], three-layer structures, such as the metal film bounded by dielectrics[4] or the dielectric film bounded by metals[5], are also easily handled analytically yielding a dispersion (transcendental) equation, and structures involving many (more than three) layers leads naturally to the transfer matrix method[6], which is an analytical technique also yielding a dispersion equation. The analysis of such waveguides can be viewed as generating "exact" results, within the accuracy with which the roots of the dispersion equation are obtained, or within the accuracy of the numerical representation used by the computer.

In contrast, 2D SPP waveguides, described by two transverse dimensions, cannot be handled analytically. A numerical method, involving discretisation in the transverse domain must be applied to determine the modes. Many SPP waveguides have been analysed using a few popular numerical methods, principally the method of lines (MoL), the finite-element method (FEM), the finite-difference method (FDM), and the finite-difference time-domain (FDTD) method. For example, the rectangular cross-section metal stripe[7-23] has been analysed using the MoL[7-10,14,20], the FEM[11,13,17,19,21,22,23] and the FDM[12,15,16,18], and the square cross-section metal stripe[24,25] has been analysed using the MoL[24] and the FEM[25]. The metal channel (V-channel or V-groove)[26-30] has been analysed using a Green's function approach[26], the FDTD[27-29], the multiple multipole method (MMP)[29], and the FEM[30]. The metal trench (slot or U-channel)[31-35], has

been analysed using the FDM[31,33-35] and the FDTD[32,33]. The metal wedge (corner)[7,8,36-38,30] has been analysed using the MoL[7,8], the FDTD[37,38] the MMP[38] and the FEM[30]. A few studies of bend modes along the metal stripe have also been reported[39,40,19,21] using the MoL[39,40] and the FEM[19,21].

Regardless of the numerical method used, the convergence of the results with respect to the discretisation scheme applied must be well-understood in order to claim accuracy in the computations. It is generally expected that modal results presented in the literature should be sufficiently accurate (and converged) to allow operating principles to be understood and conclusions drawn, and to allow comparisons with (dis)similar structures in the literature. Indeed, many authors state having assessed the convergence of their method, and some estimate the accuracy of their results. However, detailed convergence and accuracy studies have yet to be reported in the broad literature for any of the methods used to date to analyse 2D SPP waveguides. It seems important to do so at this time, given the ongoing vigorous research activity occurring within this field.

Thus, we report and compare in this paper the convergence and accuracy of two methods commonly employed to analyse 2D SPP waveguides, the MoL and the FEM, by applying both methods to a few important structures, including the metal slab, the metal stripe and the 90° metal corner. Additionally, we assess the convergence and accuracy of the MoL for curves via application to the curved metal stripe.

2. Waveguides and methods

2.1 Waveguides

Fig. 1 gives sketches of the SPP waveguides used to assess the convergence and accuracy of the numerical methods. Fig. 1(a) depicts a metal stripe of width w, thickness t and permittivity ε_2, embedded in an optically infinite homogeneous dielectric of permittivity ε_1. Fig. 1(b) shows an isolated 90° metal corner (ε_2) bounded by a conformal and optically large homogeneous dielectric (ε_1). The corner is obtained from the stripe of Fig. 1(a) by letting $w, t \rightarrow \infty$. The Cartesian coordinate system used for the analysis is also sketched on both figures. Figs. 1(c) and (d) depict in cross-sectional and top views, a metal stripe, such as that of Fig. 1(a), but curved at a radius of curvature r_0 in the plane of the stripe. This structure is described and analysed in cylindrical coordinates, also sketched on these figures.

An $e^{+j\omega t}$ time dependence is assumed throughout. In the case of the straight structures of Figs. 1(a) and (b), the modes propagate in the $+z$ direction according to $e^{-\gamma_z z}$. The complex propagation constant γ_z expands as $\gamma_z = \alpha + j\beta$ where α and β are the attenuation and phase constants, respectively. The normalised propagation constant is given by $\gamma_z/\beta_0 = \alpha/\beta_0 + j\beta/\beta_0$ where $\beta_0 = 2\pi/\lambda_0 = \omega/c_0$ is the phase constant of plane waves in vacuum, λ_0 the wavelength in vacuum, and c_0 the speed of light in vacuum. The relative permittivity of the metal expands into real and imaginary parts as $\varepsilon_{r,2} = -\varepsilon_R - j\varepsilon_I$. In the case of the curved structure of Figs. 1(c) and (d), the modes propagate in the $+\phi$ direction according to $e^{-\gamma_\phi \phi}$ where $\gamma_\phi = \alpha_\phi + j\beta_\phi$.

The structures depicted in Fig. 1 were selected because the metal stripe (Figs. 1(a), (c) and (d)) is of current interest, and the metal corner (Fig. 1(b)), being more generic, is a constituent part of the stripe but also of interest as a waveguide in its own right (i.e.: as a wedge waveguide).

Modelling SPP waveguides in general, and those of Fig. 1 in particular, raises serious challenges in that: (i) a large difference between the permittivities of the metal and the surrounding dielectric exists (typically, $\varepsilon_R \sim 10$ to 100 and $\varepsilon_{r,I} \sim 2$); (ii) losses should not be ignored ($\varepsilon_I \sim 10$); (iii) structures having a large aspect ratio or divergent cross-sectional dimensions are often of interest (e.g.: $w >> t$ for the metal stripe); (iv) some mode field components appear to diverge near metal corners; and (v) some modes are highly localised to the metal/dielectric interfaces, whereas (vi) other modes spread over a large area, sometimes in the same waveguide (e.g.: metal stripe with small t). These modelling difficulties further motivate the need for the present study.

2.2 MoL

The MoL formulated in rectangular coordinates[41-44] was used for modelling the straight waveguides (Figs. 1(a) and (b)). The underlying principle in the MoL is to discretise M-1 dimensions of an M-dimensional domain, and to apply analytic solutions along the remaining dimension. For a 2D domain such as a waveguide cross-section, a 1D discretisation only is applied, with the fields determined analytically along the remaining dimension. The MoL is therefore an accurate and efficient numerical technique due to the analytic forms embedded in the method. It is also fully vectorial, yielding, if desired, the distribution of a mode's six field components over the waveguide cross-section. The specific MoL scheme applied here is described in Ref. 43, simplified for isotropic media as described in Refs. 8 and 44, yielding essentially the same formulation as described in Ref. 41 for dielectric waveguides.

Fig. 2(a) gives a typical MoL discretisation. Regions I and III are discretised using a non-equidistant line spacing, increasing geometrically as the lateral boundaries are approached. Region II is discretised using an equidistant line spacing, with the distance between successive H or E lines set to h_{min}, the minimum spacing in the scheme. The lateral boundary conditions are shown here as magnetic walls (*mw*'s) and the top and bottom boundary conditions as electric walls (*ew*'s). The E_x, H_y and H_z field components are known on the H line system, whereas the H_x, E_y and E_z fields are known on the E line system.

Open structures are modelled by placing both (or either) of the top and bottom boundaries of the domain at infinity (mathematically in the analytic forms), and by placing both (or either) of the lateral boundaries far away from the mode, or by using lateral absorbing boundary conditions, based, for example, on the one-wave wave equation[42]. Handling open structures properly is essential if weakly guiding structures or cut-off conditions are to be handled accurately.

The MoL formulated in cylindrical coordinates[45,39] was used for modelling the curved waveguides, with the analytic forms applied along the z axis, and the spatial discretisation taken along the ρ axis (Figs. 1(c) and (d)) in a scheme that is similar to that depicted in Fig. 2(a) except that it is equidistant throughout.

An absorbing boundary condition[42,45], positioned on the radiating side of the bend (right side in Fig. 1 (c)) is required and used. The MoL for bends is also fully vectorial, providing the same computational advantages as the MoL for straight waveguides. The MoL for bends can also model straight waveguides by letting $r_0 \rightarrow \infty$.

The MoL is well-suited to the divergent dimensional scales present in many SPP waveguides, as the analytic forms are applied along the vertical axis, over features that are often nanometric in scale, and the discretisation is taken along the horizontal axis, over features that are often larger, for instance, micrometric in scale.

2.3 FEM

The straight waveguides are also modelled using a fully vectorial finite element method (FEM) available commercially[46]. In the FEM, both dimensions of the waveguide cross-section are discretised, so the method requires more computational effort to achieve accuracies comparable to the MoL. (Similar comments would apply to the application of the FDM).

Fig. 2(b) shows a portion of an example FEM discretisation scheme applied to the metal stripe of Fig. 1(a). The mesh is roughly uniform within the metal, and in the dielectric region near the metal, with the minimum spacing between nodes h_{min} being approximately constant over these regions. The lateral boundary condition is shown here as a magnetic wall (*mw*) and the bottom boundary condition as an electric wall (*ew*). The inset shows the right edge of the metal stripe in expanded view. Fig. 2(c) shows a refinement of the mesh depicted in Fig. 2(b), reducing the spacing between nodes by about half.

2.4 Extrapolation

Computations are expected to converge to more accurate values as h_{min} decreases as long as round-off errors do not become significant. The full convergence history of a computation is useful in that it can be used to guess a more accurate value by extrapolation, and to infer the accuracy of the computation. Richardson's recursive extrapolation formula[47]:

$$E_p(h_{\min}) = \frac{2^p E_{p-1}(h_{\min}) - E_{p-1}(2h_{\min})}{2^p - 1} \tag{1}$$

conveniently makes use of a series of initial computations E_0, obtained with a series of discretisations generated by successively halving h_{min}. Extrapolation to the p^{th} level is possible for a series of $p+1$ computations.

The reliability of the extrapolation increases if the results converge smoothly (preferably monotonically) with decreasing h_{min}. It is known that the MoL converges monotonically with decreasing h_{min} in the case of an equidistant discretisation[41]. As will be apparent from the results given in the following sections, the convergence is also essentially monotonic for both the MoL and the FEM with non-equidistant discretisations, as long as the discretisation remains approximately equidistant (or uniform) over the area

where the mode fields are significant. This is the rationale for using discretisations such as those given in Fig. 2.

3. Metal slab

We consider first the metal slab, obtained from Fig. 1(a) by setting $w = \infty$. This waveguide supports two purely bound SPP modes, denoted s_b and a_b, having symmetric and asymmetric distributions along y for their E_y field component, respectively[4]. The confinement and attenuation of the s_b mode decrease with decreasing t, whereas the opposite holds for the a_b mode with decreasing t. At small t the modes are therefore often referred to as the long-range SPP (LRSPP) and short-range SPP (SRSPP), respectively.

The modes in this 1D structure exhibit no variation over x so exact results (in the sense described in the introduction) can be obtained either by solving the transcendental equations for the modes[4], by applying the transfer matrix method[6], or by applying the MoL which also yields exact results for 1D structures when they are described along the analytic dimension (i.e.: along y in Fig. 2(a)). The exact results, once generated can be used as a basis of comparison.

Figs. 3(a) and (b) give the (exact) normalised attenuation and effective index of the s_b and a_b modes in the metal slab ($w = \infty$) computed using the MoL, for $\lambda_0 = 633$ nm, $\varepsilon_{r,1} = 4$ and $\varepsilon_{r,2} = -19\text{-j}0.53$, as a function of t. The permittivities selected originate from Refs. 4 and 8, and are representative of Si_3N_4 and Ag, respectively. For reference, the distribution of the normalised $\mathrm{Re}\{E_y\}$ of the a_b and s_b modes for t = 100 nm are shown as the top and bottom insets in Fig. 3(a), respectively.

The metal slab was then rotated 90° such that the line system of the MoL ran across its thickness. In this orientation, the MoL no longer yields exact results but rather exhibits convergence with decreasing h_{min}. Half symmetry was exploited via the left boundary, and the top and bottom boundaries were placed at infinity. Regions I and II were equidistant (Fig. 2(a)), and Region III, which began at a distance of $t/2$ beyond the metal, was non-equidistant with a geometric expansion parameter of 1.15 used to position the right boundary far from the mode.

Figs. 4(a) and (b) give the normalised attenuation and effective index of the s_b and a_b modes for t = 100 nm, computed in this manner, as a function of h_{min}. Exact values from Fig. 3 are plotted at $h_{min} = 0$. The percentage errors relative to the exact values are plotted in Fig. 4(c). As noted from this figure, convergence to an error of better than ±0.1% is readily achieved for $h_{min} \cong 1.4$ nm, obtained with 35 lines over $t/2$ and a total of about 100 lines. This bodes well for modeling 2D SPP waveguides, which have mode fields that do vary over x, and thus over the line system.

Figs. 5(a) and (b) give the normalised attenuation and effective index of the s_b and a_b modes of the same metal slab as a function of discretisation, but computed using the FEM, exploiting half symmetry. Again, exact values from Fig. 3 are plotted at $h_{min} = 0$, and the percentage errors relative to the exact values are plotted in Fig. 5(c). Convergence to an error of better than ±0.001% occurs very rapidly, with a

discretisation as coarse as $h_{min} \cong 10$ nm. The errors are lower than those plotted in Fig. 4(c) for the rotated structure analysed with the MoL, but it is emphasized that the results obtained with the MoL for the un-rotated structure (Fig. 3) are exact. Nevertheless, readily achieving errors as low as this bodes very well for modeling 2D SPP waveguides with the FEM.

4. Metal stripe

We consider now the metal stripe depicted in Fig. 1(a). In general, the metal stripe supports numerous purely bound SPP modes[7,8], each having a characteristic E_y field distribution along x, and either a symmetric or an asymmetric distribution along y. Four fundamental modes exist, one for each quarter symmetry, as well as higher order modes which appear as w increases. All six field components are present in all modes, although many are primarily TM in character for $w >> t$. At small t, the modes can be classified as LRSPPs or SRSPPs, following the metal slab ($w = \infty$). (It should be noted that the modes become significantly more complex in an asymmetric metal stripe, where the permittivity above the stripe differs from that below[9,10].).

Figs. 6(a) and (b) give the normalised attenuation and effective index of three modes, the ss_b^0, ss_b^1 and sa_b^0 modes[8], for $w = 1$ μm, $\lambda_0 = 633$ nm, $\varepsilon_{r,1} = 4$ and $\varepsilon_{r,2} = -19\text{-}j0.53$ as a function of t. The computations were performed using the MoL exploiting quarter symmetry and using two discretisations ($h_{min} \cong 10$ and 5 nm), with Regions I and II being equidistant and Region III being non-equidistant (geometric expansion parameter of 1.12). Curves extrapolated from these results using Eq. (1) are also plotted. For the purpose of discussion, Fig. 7 shows the distribution of the normalised $\mathrm{Re}\{E_y\}$ of these modes in this waveguide for $t = 100$ nm, as computed using the MoL with $h_{min} \cong 10$ nm. The ss_b^0 and sa_b^0 modes are fundamental, and the ss_b^1 mode is the first higher order mode exhibiting E_y field symmetry along y. These modes are representative of others supported by this structure which are either highly localised to the metal corners and edges or distributed over a larger area. The convergence characteristics of these three modes are therefore representative of other modes in the stripe.

From Fig. 6, it is noted that the results for the ss_b^0 and sa_b^0 modes converge slowly and similarly at large t (> 75 nm), but not at small t where convergence of the ss_b^0 mode occurs much more rapidly with all three curves overlapping almost perfectly for $t < 50$ nm. At large t, both modes are highly localised to the metal corners, as shown in Figs. 7(a) and (c), so convergence is slower. This localisation persists with decreasing t for the sa_b^0 mode, but not for ss_b^0 mode which becomes less localised with decreasing t. Indeed, at small t, the ss_b^0 mode is long-range and less confined, having mode fields that cover a large cross-sectional area[8].

Similarly, rapid convergence occurs for the ss_b^1 mode, given its field distribution (Fig. 7(b)). However, this mode cuts-off at small t, which challenges the discretisation differently, in that it must remain dense enough near the stripe to accurately capture sharp field variations at large t, yet allow the

mode its full expansion as t decreases. This latter point is especially important if the cut-off thickness is to be determined accurately. Given that a mode at cut-off expands infinitely into the dielectric, then the boundaries must be positioned at or near infinity or absorbing boundaries must be used.

As w and t increase, the ss_b^0 and sa_b^0 modes (and the other two fundamental modes[8], as_b^0 and aa_b^0) evolve into the mode of an isolated 90° corner[8]. To illustrate this, we plot on Fig. 6 the results computed for the corresponding corner (using similar discretisations) on the right limit of the graphs, and zoom in on these regions in inset. The ss_b^0 and sa_b^0 modes are noted to approach the corresponding values for the corner at each discretisation, but the width and thickness of the stripe here (w = 1 μm, t = 200 nm) are such that come coupling between the corners remain, so the curves do not align perfectly with the corresponding corner results. (The corner is discussed in greater detail in the next section.)

Figs. 8(a) and (b) plot the normalised attenuation and effective index of the ss_b^0 and ss_b^1 modes for t = 100 nm as a function of discretisation, capturing the convergence of a highly localized mode (ss_b^0, Fig. 7(a)) and of one that has fields distributed over a larger area (ss_b^1, Fig. 7(b)). The computations were performed using the MoL, exploiting quarter symmetry, with Regions I and II being equidistant and Region III being non-equidistant (geometric expansion parameter of 1.12) and starting ~0.1 μm from the right edge of the metal stripe. The FEM was also used, exploiting quarter symmetry, with approximately equidistant (uniform) meshes in the region of the stripe (e.g.: Figs. 2(b) and (c)). The extrapolated values, plotted at $h_{min} = 0$, were computed via Eq. (1) using results obtained with discretisations that were successively halved. Figs. 8(c) and (d) plot the percentage errors relative to the extrapolated values for the MoL and FEM, respectively. These errors should be regarded as *anticipated errors* rather than actual errors since they are relative to extrapolated values.

The convergence of both methods is smooth because the discretisations remain approximately equidistant over most of the mode area (as argued in Sub-section 2.4). The extrapolated values are all credible. The ss_b^0 mode converges more slowly than the ss_b^1 mode due to greater field localization near the corners for the former. The normalised attenuation converges more slowly than the effective index for both modes and both methods. Both the MoL and the FEM converge to similar anticipated errors for a comparable h_{min}, with slightly lower errors observed for the FEM. Convergence to within ±2% is achieved with both methods for $h_{min} \cong 5$ nm, except for the normalised attenuation of the ss_b^0 mode, which remains in error by about 20% and 10% for the MoL and FEM, respectively. The numerical effort required to compute these results is lower for the MoL than for the FEM, but is quite manageable in both cases using recent model personal computers.

Table 1 summarises the extrapolated normalised attenuation and effective index of the ss_b^0 and ss_b^1 modes plotted at $h_{min} = 0$ in Figs. 8(a) and (b). The percentage difference (relative to the MoL) is quite small, except for the normalised attenuation of the ss_b^0, which is not as well converged (as mentioned above).

The results marked by the filled symbols in Figs. 8(a)-(c) were computed for the ssb^0 mode by rotating the same metal stripe by 90° relative to the MoL discretisation scheme such that the lines ran across its thickness. Quarter symmetry was exploited, the discretisation design was similar to that of the other orientation, and h_{min} was set to 2 nm. The results are well-aligned with the convergence curves as observed, suggesting that analyzing the stripe in either orientation yields essentially the same accuracy. However, only 66 lines were needed to model the stripe in this orientation compared to 210 lines for the most accurate case in the other orientation ($h_{min} \cong 3$ nm), resulting in significantly less numerical effort.

5. Metal corner

We consider now the 90° metal corner depicted in Fig. 1(b). The metal corner supports one purely bound SPP mode, having mode fields that are localised at the corner and that decay exponentially away in all directions. All six field components are present in the mode, and the main transverse electric field components, E_x and E_y, are equally important (same peak values), so the mode is not TM in character. The mode satisfies magnetic wall symmetry along the plane running through the apex at 45° from the horizontal.

In the case of the MoL, the corner was positioned in the centre of the equidistant Region II (Fig. 2(a)), with non-equidistant Regions I and III starting 0.2 μm away from the corner on either side (geometric expansion parameter of 1.12). In the case of the FEM, the discretisations were approximately uniform near the corner and along the edges in the immediate vicinity of the mode. The corner was not rounded.

Fig. 9 shows the normalised $\mathrm{Re}\{E_y\}$ of the corner mode for $\lambda_0 = 633$ nm, $\varepsilon_{r,2} = -19\text{-}j0.53$ and $\varepsilon_{r,1}$ ranging from 1 to 4 computed using the MoL with $h_{min} = 10$ nm. The mode is observed to become more localised to the corner as $\varepsilon_{r,1}$ increases (all other variables and the discretisation remaining constant).

Fig. 10 shows the normalised attenuation and effective index of the mode as a function of discretisation for the same values of $\varepsilon_{r,1}$. The computations were performed using the MoL and the FEM. The extrapolated values, plotted at $h_{min} = 0$, were computed via Eq. (1). The convergence is smooth in all cases (although not monotonic for the MoL in Fig. 10(b) because the mode fields remain significant in the non-equidistant regions in this case - see Fig. 9(a)). The extrapolated values are all credible, and they agree reasonably well for both methods.

Figs. 11(a)-(b) and 11(c)-(d) plot the associated percentage errors relative to the extrapolated values (i.e.: the *anticipated errors*) for the MoL and FEM, respectively. For both methods, the results converge more slowly as $\varepsilon_{r,1}$ increases, due to the increasing localisation of the mode to the corner, as noted earlier. The normalised attenuation converges more slowly than the effective index for both methods. Both the MoL and the FEM converge to similar anticipated errors for a comparable h_{min}, with slightly lower errors observed for the FEM. For $\varepsilon_{r,1} = 4$ (worse case), convergence of the effective index to better than ±2% is achieved with both methods for $h_{min} \cong 5$ nm, but the normalised attenuation remains in error by

about 20% and 10% for the MoL and FEM, respectively. The numerical effort required to compute these results is lower for the MoL than for the FEM, but is manageable in both cases.

The precise behaviour of electrodynamic fields scattered by a dielectric wedge, very near the edge of the wedge, remains the subject of ongoing research (e.g.: Ref. 48 and references therein). However, it is apparent from studies conducted to date that the transverse electric and magnetic fields diverge near the edge of the wedge, but that the longitudinal fields remain finite[48]. One could then surmise that the transverse SPP mode fields supported by a 90° metal corner should also diverge as the corner is approached, a hypothesis that is further encouraged (but not verified) by the field distributions of Figs. 7 and 9. Field divergence near corners causes slow convergence in the computation of modes in dielectric waveguides, especially for strongly guiding structures[49]. This point is consistent with this study, in that the slowest convergence occurred for the most strongly guided modes (e.g.: the SPP on the metal corner bounded by a dielectric of $\varepsilon_{r,1} = 4$). It is noteworthy, however, that (i) both numerical methods converge, (ii) that they converge to very similar extrapolated propagation constants (Figs. 10), and (iii) that the extrapolated values are approached from opposite directions, from the top for the MoL and from the bottom for the FEM, essentially "cornering" the values. So even if the transverse fields diverge near the corner, convergence of mode computations, although slow, evidently still occurs. This is sensible considering that the fields might diverge according to a similar power law as dielectric corners[48], limiting the divergence to an area considerably smaller than the mode size. The rate of convergence also depends on the angle of the metal corner (90° here), so convergence studies should be undertaken for other angles, for example, pertaining to the metal channel or wedge.

6. Curved metal stripe

We consider now the curved metal stripe depicted in Figs. 1(c)-(d). As outlined in Sub-section 2.2, the structure was analysed using the MoL for curves formulated in cylindrical coordinates, using an equidistant discretisation along ρ and an absorbing boundary condition based on the one-way wave equation on the right boundary. The left boundary was positioned far from the stripe and the top and bottom boundaries were placed at infinity (mathematically, in the analytic forms applied along z).

Figs. 12(a) and (b) plot the normalised attenuation and effective index of the $ss_b{}^0$ mode for $w = 1$ μm, $t = 15$ nm, $\lambda_0 = 633$ nm, $\varepsilon_{r,1} = 4$ and $\varepsilon_{r,2} = -19\text{-}j0.53$ as a function of the discretisation, for two radii of curvature, $r_0 = \infty$ (1 m in the computations) and $r_0 = 124.5$ μm. The latter corresponds to the optimal radius for this structure, minimising the insertion (propagation and radiation) loss of the curve[39]. The extrapolated values, plotted at $h_{min} = 0$, were computed via Eq. (1). The convergence is smooth in all cases and the extrapolated values are credible.

Fig. 12(c) plots the associated percentage errors relative to the extrapolated values (i.e.: the *anticipated errors*). The convergence is very rapid, with the normalised attenuation and the effective index both converged to better than ±2% at $h_{min} = 20$ nm for both radii of curvature. The $ss_b{}^0$ mode is long-range

for these stripe dimensions, and so its mode fields cover a large cross-sectional area. Convergence is therefore expected to be rapid, as discussed in Section 3 (and observed in Fig. 6 for this mode at small t).

Fig. 13 plots the distribution of the normalised $\mathrm{Re}\{E_z\}$ of the mode for r_0 = 124.5 μm, computed with $h_{min} \cong 50$ nm. Radiation along the outside of the curve is evident, although not too strong at this radius, but it increases as r_0 decreases beyond this value. The need for an absorbing boundary condition is clear. However its quality affects the accuracy of the results, and in fact can ultimately set the accuracy if the discretisation error is sufficiently reduced.

In order to explore the impact of this boundary on the accuracy we plot in Figs. 14(a) and (b) the normalised attenuation and effective index for the curved stripe at r_0 = 124.5 μm as a function of the distance between the right edge of the stripe and the boundary. The computations were performed with $h_{min} \cong 30$ nm. Clearly, the results are sensitive to the location of the absorbing boundary, which would not be the case if it were perfect. Evidently, the boundary should be placed some distance away from the stripe, but, perhaps counter-intuitively, placing it increasingly far away does not improve the accuracy. The oscillatory portion of each plot is shown in expanded view in inset. The peak-to-peak variation is about 2×10^{-5} for both the normalised attenuation and the effective index, representing errors of about 2% and 5×10^{-4}%, respectively, relative to the values at the mid-point. Comparing these with the anticipated errors for r_0 = 124.5 μm at $h_{min} \cong 30$ nm (Fig. 12(c)), reveals that the accuracy of the normalised attenuation is in fact limited by the absorbing boundary condition. (The absorbing boundary was positioned 2.2 μm from the right edge of the stripe in the computations of Fig. 12.) The amplitude of the oscillations in Fig. 14 increase as r_0 decreases due to increasing radiation from the curve.

7. Summary and concluding remarks

The convergence and accuracy of two vectorial numerical methods commonly employed to analyse 2D SPP waveguides, the MoL (in-house code) and the FEM (available commercially), were assessed by applying both methods to a few important structures, including the metal slab, the metal stripe and the 90° metal corner, and computing the characteristics of some modes supported therein.

Non-equidistant discretisations were used with both methods, however, the discretisations were densest and approximately equidistant (uniform) over most of the area covered by the mode fields. Successive refinements (densification) of a discretisation maintained the "pattern" of the initial one. Following this strategy yielded smooth monotonic convergence plots as a function of the minimal spacing (h_{min}) for both methods, from which more accurate results were then reliably extrapolated. Anticipated errors were then computed relative to the extrapolated results as a function of h_{min}.

Both methods yielded similar anticipated errors at a comparable h_{min}, with the FEM yielding slightly lower errors but the MoL requiring less computational effort. Convergence was slower for highly confined modes, particularly for modes having fields localised near corners. The error in the normalised attenuation was consistently larger than that in the effective index, probably because the normalised

attenuation is significantly smaller than the effective index. For all of the modes and waveguides investigated, convergence to within an anticipated error of ±2% was readily achieved with both methods ($h_{min} \cong 5$ nm), except for the normalised attenuation of modes that are highly localised to corners which remained in error by 10 to 20%.

Importantly, maintaining smooth convergence allowed reliable extrapolation to more accurate results. For instance, the percentage difference between the extrapolated results computed from the FEM and MoL convergence histories ranged from 3.75 to 0.012% for modes of the metal stripe.

The convergence and accuracy of the MoL for curves was also investigated by application to the curved metal stripe. It was found that the absorbing boundary condition used to terminate the boundary along the outside of the curve (i.e.: the radiating side) introduces errors, and that these errors could limit the accuracy of the results, particularly of the normalised attenuation.

References

[1] H. Raether, *Surface Plasmons on Smooth and Rough Surfaces and on Gratings* (Springer, Berlin, 1988)

[2] W. L. Barnes, A. Dereux, and T. W. Ebbesen, *Nature* 424, 824 (**2003**)

[3] S. A. Maier and H. A. Atwater, *J. Appl. Phys.* 98, 011101 (**2005**)

[4] J. J. Burke, G. I. Stegeman, and T. Tamir, *Phys. Rev. B* 33, 5186 (**1986**)

[5] J. A. Dionne, L. A. Sweatlock, H. A. Atwater and A. Polman, *Phys. Rev. B* 73, 035407 (**2006**)

[6] C. Chen, P. Berini, D. Feng, S. Tanev, V. P. Tzolov, *Opt. Express* 7, 260 (**2000**)

[7] P. Berini, *Opt. Lett.* 24, 1011 (**1999**)

[8] P. Berini, *Phys. Rev. B* 61, 10484 (**2000**)

[9] P. Berini, *Opt. Express* 7, 329 (**2000**)

[10] P. Berini, *Phys. Rev. B* 63, 125417 (**2001**)

[11] I. G. Breukelaar, M.A.Sc. Thesis, University of Ottawa (**2004**)

[12] S. J. Al-Bader, *IEEE J. Quant. Electron.* 40, 325 (**2004**)

[13] M. P. Nezhad, K. Tetz, Y. Fainman, *Opt. Express* 12, 4072 (**2004**)

[14] P. Berini, R. Charbonneau, N. Lahoud and G. Mattiussi, *J. Appl. Phys.* 98, 043109 (**2005**)

[15] R. Zia, A. Chandran, M. L. Brongersma, *Opt. Lett.* 30, 1473 (**2005**)

[16] R. Zia, M. D. Selker, and M. L. Brongersma, *Phys. Rev. B* 71, 165431 (**2005**)

[17] I. Breukelaar, R. Charbonneau and P. Berini, *J. Appl. Phys.* 100, 043104 (**2006**)

[18] A. Hosseini, A. Nieuwoudt, Y. Massoud, *Opt. Express* 14, 7291 (**2006**)

[19] A. Degiron and D. R. Smith, *Opt. Express* 14, 1611 (**2006**)

[20] H. S. Won, K. C. Kim, S. H. Song, C.-H. Oh, P. S. Kim, S. Park, S. I. Kim, *Appl. Phys. Lett.* 88, 011110 (**2006**)

[21] A. Degiron, C. Dellagiacoma, J. G. McIlhargey, G. Shvets, O. J. F. Martin, and D. R. Smith, *Opt. Lett.* 32, 2354 (**2007**)

[22] R. Buckley and P. Berini, *Opt. Express* 15, 12174 (**2007**)

[23] M. Z. Alam, J. Meier, J. S. Aitchison, M. Mojahedi, *Opt. Express* 15, 176 (**2007**)

[24] P. Berini, U.S. Patent No. 6741782, filed 2002, awarded 2004

[25] J. Jung, T. Søndergaard and S. I. Bozhevolnyi, *Phys. Rev. B* 76, 035434 (**2007**)

[26] I. V. Novikov and A. A. Maradudin, *Phys. Rev. B* 66 035403 (**2002**)

[27] D. K. Gramotnev and D. F. P. Pile, *Appl. Phys. Lett.* 85 6323 (**2004**)

[28] D. F. P. Pile, *Appl. Phys. B* 81, 607 (**2005**)

[29] E. Moreno, F. J. Garcia-Vidal, S. G. Rodrigo, L. Martin-Moreno, S. I. Bozhevolnyi, *Opt. Lett.* 31, 3447 (**2006**)

[30] M. Yan and M. Qiu, *J. Opt. Soc. Am. B* 24, 2333 (**2007**)

[31] G. Veronis and S. Fan, *Opt. Lett.* 30, 3359 (**2005**)

[32] D. F. P. Pile, T. Ogawa, D. K. Gramotnev, Y. Matsuzaki, K. C. Vernon, K. Yamaguchi, T. Okamoto, M. Haraguchi, M. Fukui, *Appl. Phys. Lett.* 87, 261114 (**2005**)

[33] L. Liu, Z. Han, S. He, *Opt. Express 13*, 6645 (**2005**)

[34] G. Veronis and S. Fan *J. Light. Technol.* 25, 2511 (**2007**)

[35] E. Feigenbaum and M. Orenstein, *J. Light. Technol.* 25, 2547 (**2007**)

[36] L. Dobrzynski and A. A. Maradudin, *Phys. Rev. B* 6, 3810 (**1972**)

[37] D. F. P. Pile, T. Ogawa, D. K. Gramotnev, T. Okamoto, M. Haraguchi, M. Fukui, S. Matsuo, *Appl. Phys. Lett.* 87, 061106 (**2005**)

[38] E. Moreno, S. G. Rodrigo, S. I. Bozhevolnyi, L. Martin-Moreno and F. J. Garcia-Vidal, *Phys. Rev. Lett.* 100, 023901 (**2008**)

[39] P. Berini and J. Lu, *Opt. Express* 14, 2365 (**2006**)

[40] W.-K. Kim, W.-S. Yang, H.-M. Lee, H.-Y. Lee, M.-H. Lee, W.-J. Jung, *Opt. Express* 14, 13043 (**2006**)

[41] R. Pregla and W. Pascher, "The method of Lines", in "Numerical techniques for microwave and milimeter-wave passive structures", T. Itoh, Ed., (Wiley, New York, **1989**)

[42] R. Pregla, "MOL-BPM Method of lines Based Beam Propagation Method," in Progress in Electromagnetics Research Vol. 11, J. A. Kong, Ed. (EMW Publishing, Cambridge, Mass., **1995**)

[43] P. Berini and K. Wu, *IEEE Trans. Microwave Theory Tech.* 44, 749 (**1996**)

[44] P. Berini, A. Stöhr, K. Wu and D. Jäger, *J. Light. Technol.* 14, 2422 (**1996**)

[45] R. Pregla, *J. Light. Technol.* 14, 634 (**1996**)

[46] Comsol Multiphysics, Comsol Inc.

[47] R. C. Boonton Jr., "Computational Methods for Electromagnetics and Microwaves", Wiley-Interscience, **1992**

[48] E. Marx, *Radio Sci.* 42, rs6s09, (**2007**)

[49] A. S. Sudbø, *J. Light. Technol.* 10, 418 (**1992**)

Tables

Table 1: Extrapolated normalised attenuation and effective index of the ss_b^0 and ss_b^1 modes plotted at h_{min} = 0 in Figs. 8(a) and (b). The percentage difference (relative to the MoL) is also given for each.

	ss_b^0		ss_b^1	
	α/β_0	β/β_0	α/β_0	β/β_0
FEM	0.0274475	2.37941	0.00896852	2.20884
MoL	0.0285175	2.38177	0.00899414	2.20910
Difference	-3.75%	-0.099%	-0.28%	-0.012%

Figures

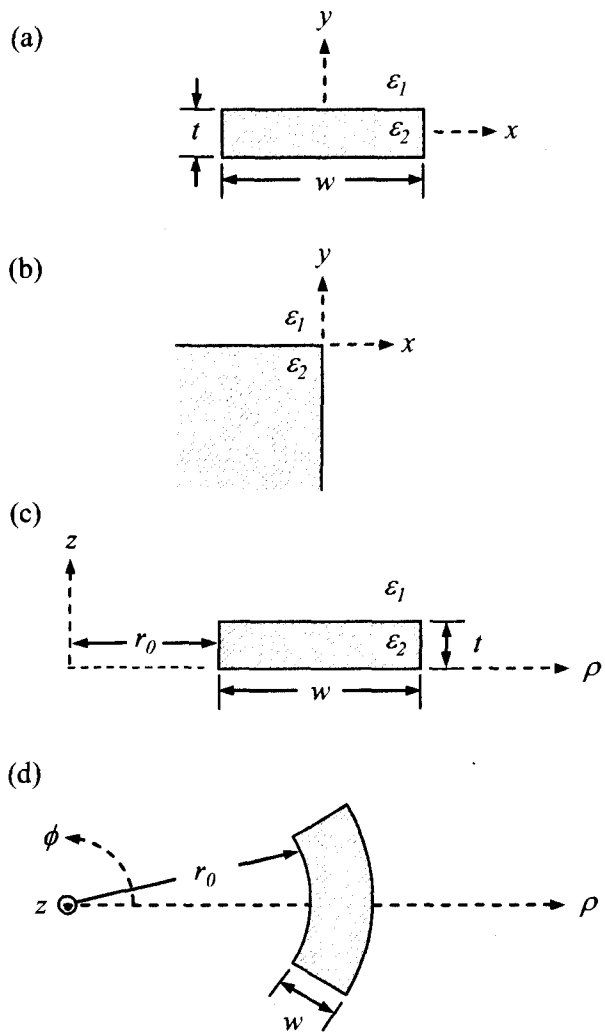

Fig. 1. Surface plasmon waveguides of interest. (a) Metal stripe of width w, thickness t and permittivity ε_2 in an optically infinite homogeneous dielectric of permittivity ε_1. (b) Isolated corner, consisting of metal (ε_2) filling all of quadrant III (southwest), bounded by a homogeneous dielectric (ε_1) filling all other quadrants. (c) and (d) Curved metal stripe (ε_2) in homogeneous dielectric (ε_1), sketched in cross-sectional and top views, respectively.

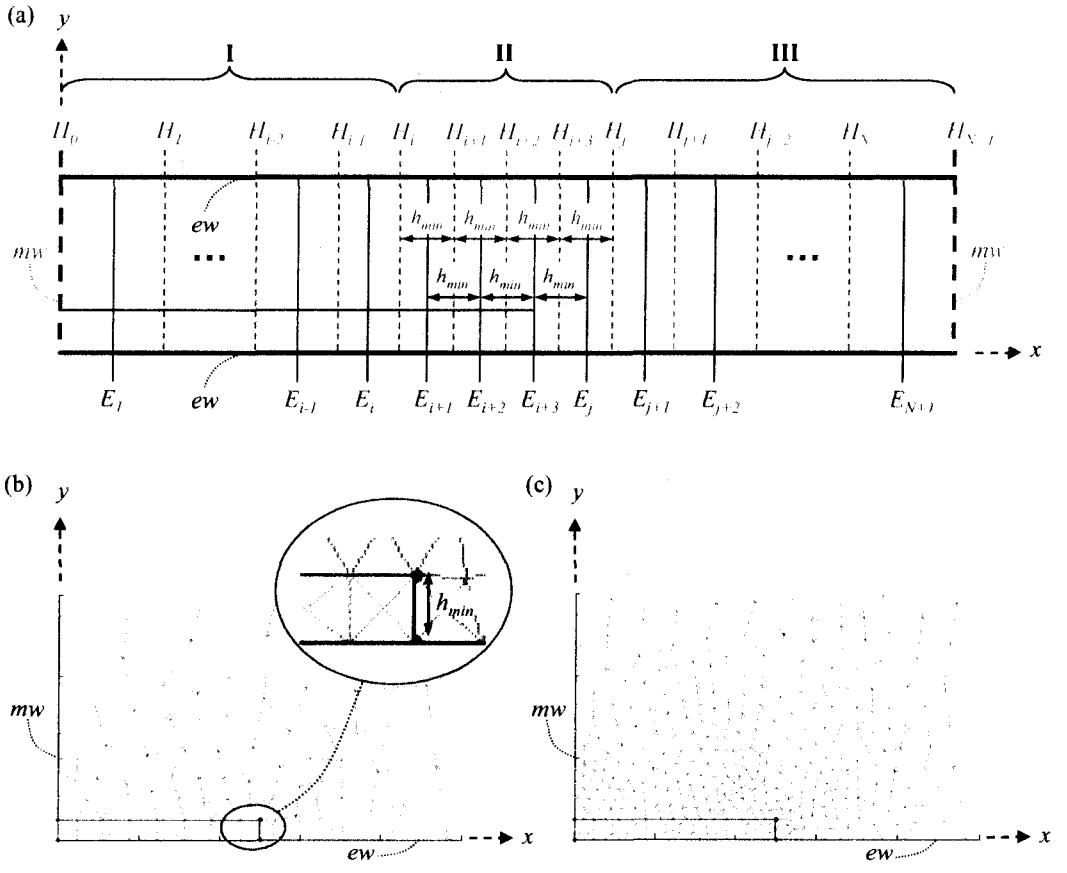

Fig. 2. (a) Example MoL discretisation scheme applied to a straight surface plasmon waveguide (e.g. Fig. 1(a) or (b)). Regions I and III are discretised using a non-equidistant line scheme, with the line spacing increasing geometrically towards the lateral boundaries. Region II is discretised using equidistant line spacing, with the distance between successive H or E lines set to h_{min}, the minimum spacing in the scheme. The lateral boundary conditions are shown here as magnetic walls (*mw*) and the top and bottom boundary conditions as electric walls (*ew*). (b) Example FEM discretisation scheme applied to the same surface plasmon waveguide. The mesh is roughly uniform within the metal, and in the dielectric region near the metal, with the minimum spacing between nodes h_{min} being approximately constant. The lateral boundary condition is shown here as a magnetic wall (*mw*) and the bottom boundary condition as an electric wall (*ew*). The inset shows the right edge of the metal stripe in expanded view. (c) Refinement of the mesh depicted in (b), reducing the spacing between nodes by about half.

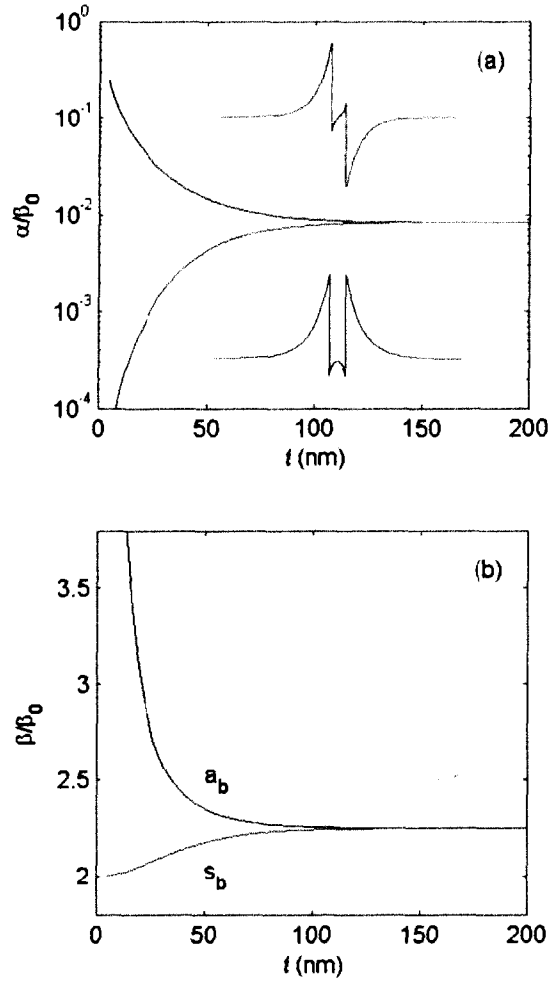

Fig. 3. (a) Normalised attenuation and (b) effective index of the s_b and a_b modes for $w = \infty$, $\lambda_0 = 633$ nm, $\varepsilon_{r,1} = 4$ and $\varepsilon_{r,2} = -19\text{-}j0.53$ as a function of t. Computations performed using the MoL. The distribution of the normalised $\mathrm{Re}\{E_y\}$ of the a_b mode is shown as the top inset in (a), and of the s_b mode as the bottom inset in (a) for $t = 100$ nm.

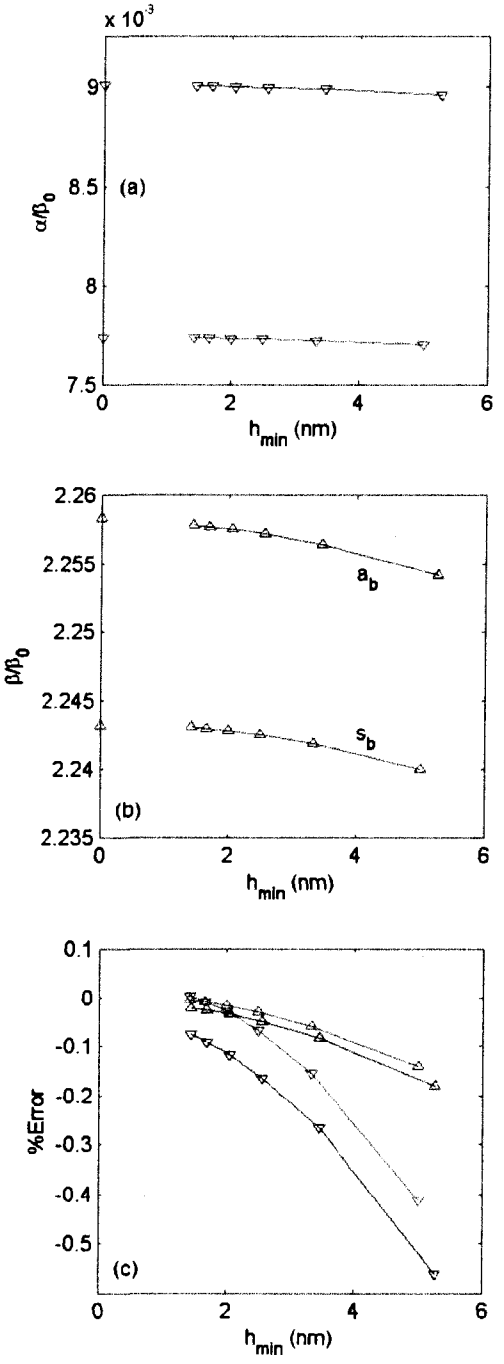

Fig. 4. (a) Normalised attenuation and (b) effective index of the s_b and a_b modes for $w = \infty$, $t = 100$ nm, $\lambda_0 = 633$ nm, $\varepsilon_{r,1} = 4$ and $\varepsilon_{r,2} = -19\text{-}j0.53$ as a function of discretisation. The computations were performed using the MoL, but with the metal slab rotated by 90° relative to the discretisation scheme. Exact values (from Fig. 3) are plotted at $h_{min} = 0$. (c) Percentage errors relative to the exact values.

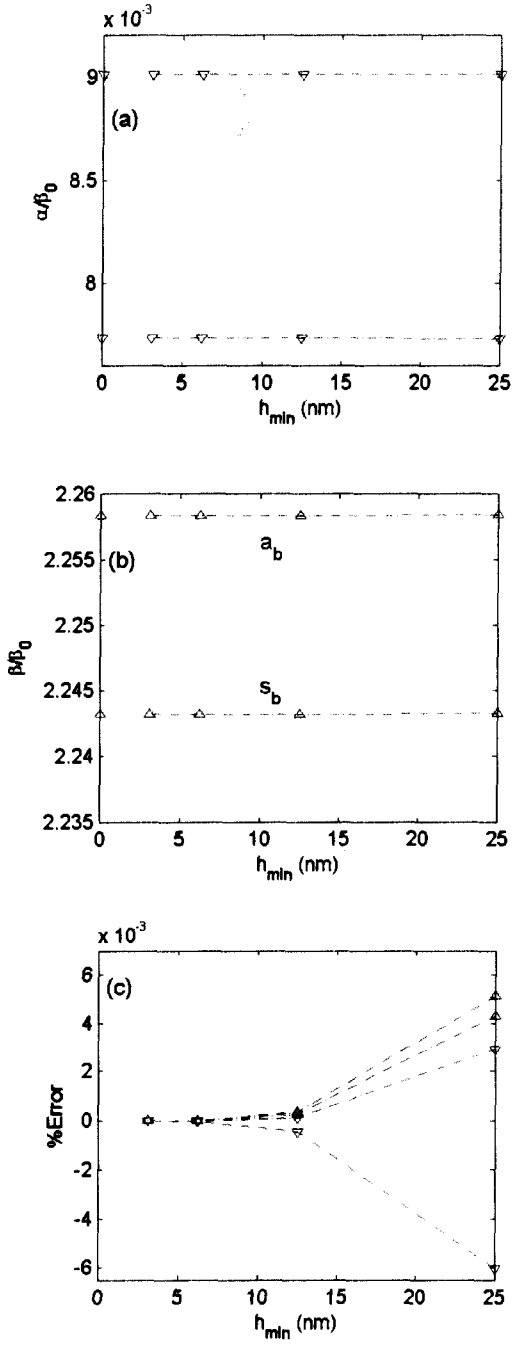

Fig. 5. (a) Normalised attenuation and (b) effective index of the s_b and a_b modes for $w = \infty$, $t = 100$ nm, $\lambda_0 = 633$ nm, $\varepsilon_{r,1} = 4$ and $\varepsilon_{r,2} = -19\text{-}j0.53$ as a function of discretisation. The computations were performed using the FEM. Exact values (from Fig. 3) are plotted at $h_{min} = 0$. (c) Percentage errors relative to the exact values.

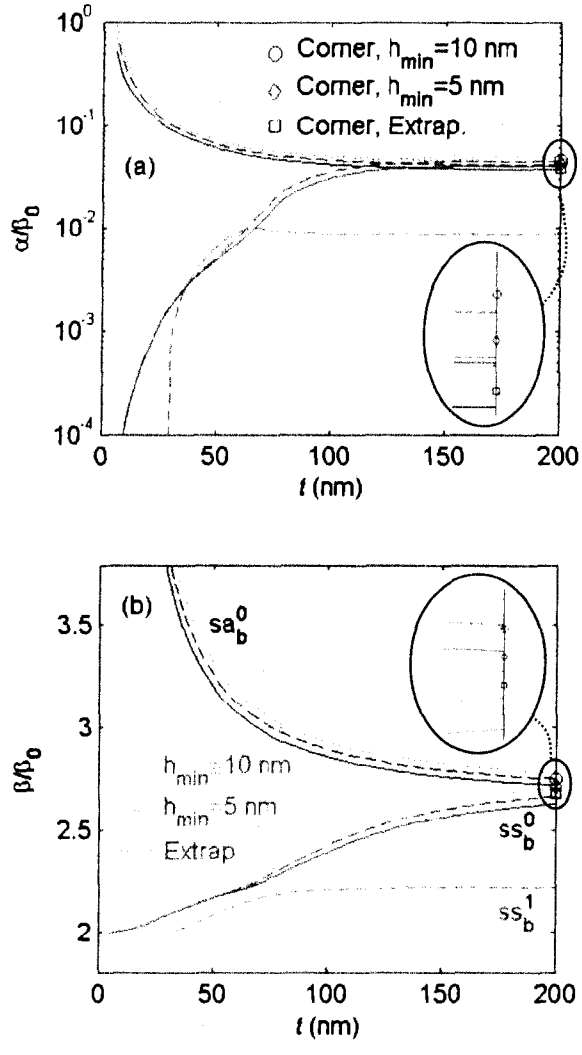

Fig. 6. (a) Normalised attenuation and (b) effective index of the ss_b^0, ss_b^1 and sa_b^0 modes for w = 1 μm, λ_0 = 633 nm, $\varepsilon_{r,1}$ = 4 and $\varepsilon_{r,2}$ = -19-j0.53 as a function of t. The computations were performed using the MoL and two discretisations ($h_{min} \cong$ 10 and 5 nm); the extrapolated curves are also plotted. The normalised attenuation and effective index of the mode supported by the corresponding isolated corner, and computed using similar discretisations (Fig. 9 (g) and (h)), are plotted as the three data points (circle, diamond and square) on the right limit of the graphs, also shown on an expanded scale as the insets.

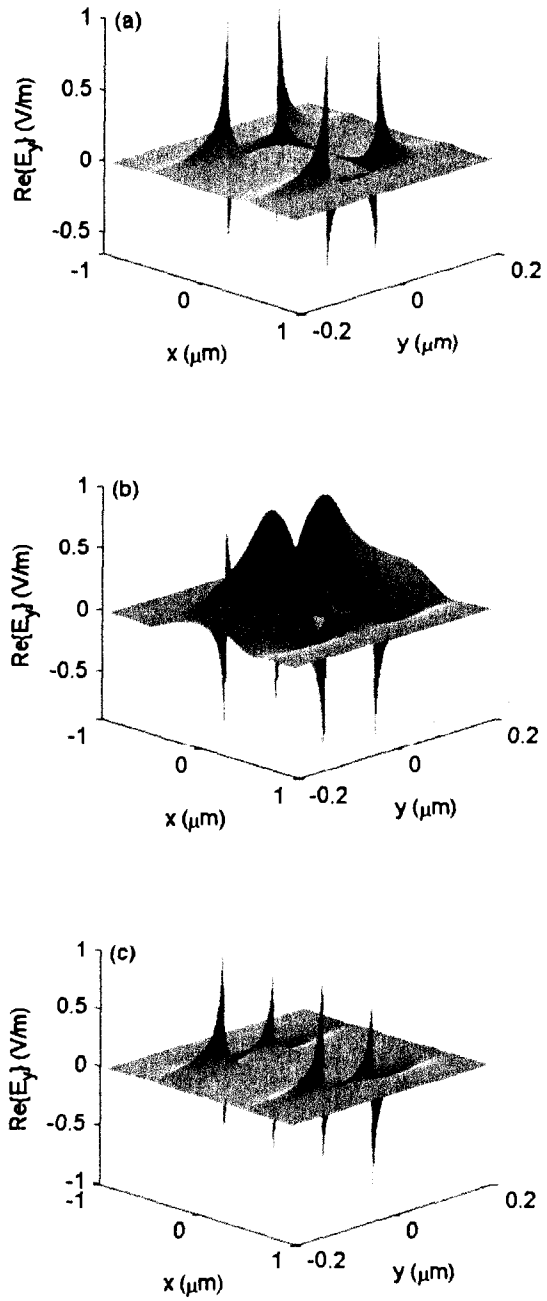

Fig. 7. Normalised Re$\{E_y\}$ of (a) the ss_b^0, (b) the ss_b^1, and (c) the sa_b^0 modes for w = 1 μm, t = 100 nm, λ_0 = 633 nm, $\varepsilon_{r,1}$ = 4 and $\varepsilon_{r,2}$ = -19-j0.53. Computations performed using the MoL with $h_{min} \cong$ 10 nm.

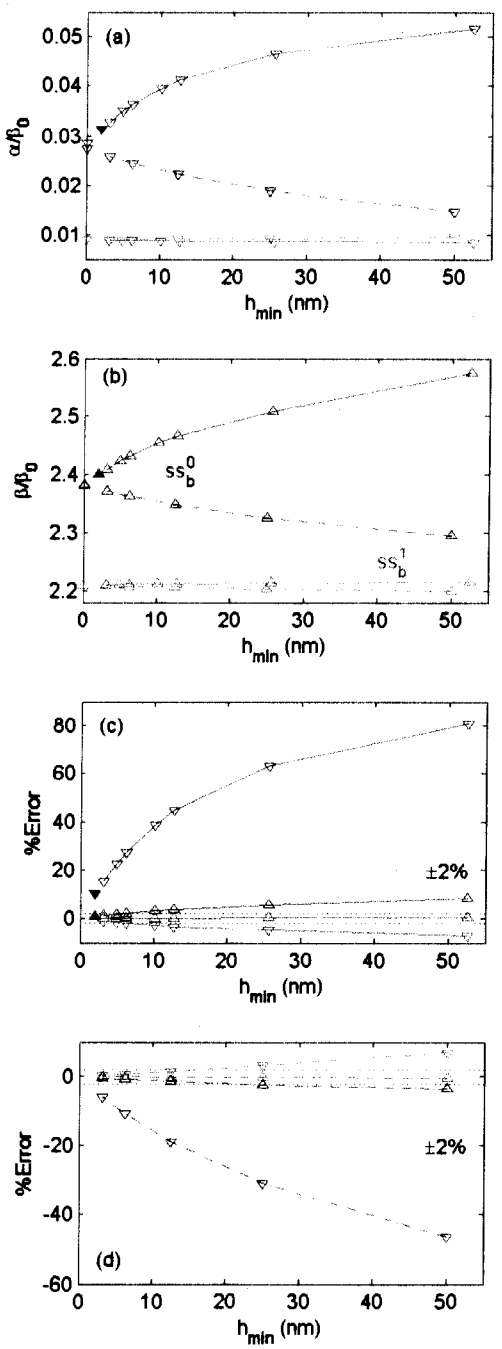

Fig. 8. (a) Normalised attenuation and (b) effective index of the ss_b^0 and ss_b^1 modes for w = 1 μm, t = 100 nm, λ_0 = 633 nm, $\varepsilon_{r,1}$ = 4 and $\varepsilon_{r,2}$ = -19-j0.53 as a function of discretisation. The computations were performed using the MoL (solid curves) and the FEM (dashed-dot curves). Extrapolated values are plotted at h_{min} = 0. (c) Percentage errors relative to the extrapolated values for the MoL; ±2% error lines are also plotted. (d) Percentage errors relative to the extrapolated values for the FEM; ±2% error lines are also plotted. The filled symbols in (a)-(c) are the results obtained by rotating the metal stripe by 90° relative to the MoL discretisation scheme.

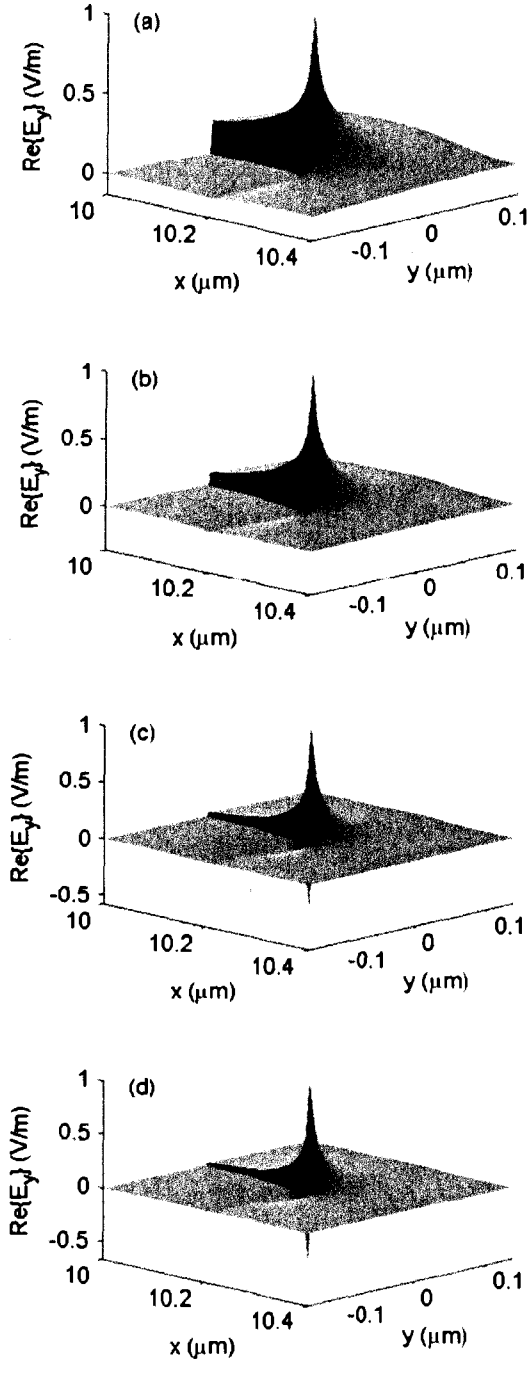

Fig. 9. Normalised Re$\{E_y\}$ of the corner mode for λ_0 = 633 nm and $\varepsilon_{r,2}$ = -19-j0.53. Computations performed using the MoL with h_{min} = 10 nm. (a) $\varepsilon_{r,1} = 1$; (b) $\varepsilon_{r,1} = 1.5^2$; (c) $\varepsilon_{r,1} = 1.9^2$; (d) $\varepsilon_{r,1} = 2.0^2$.

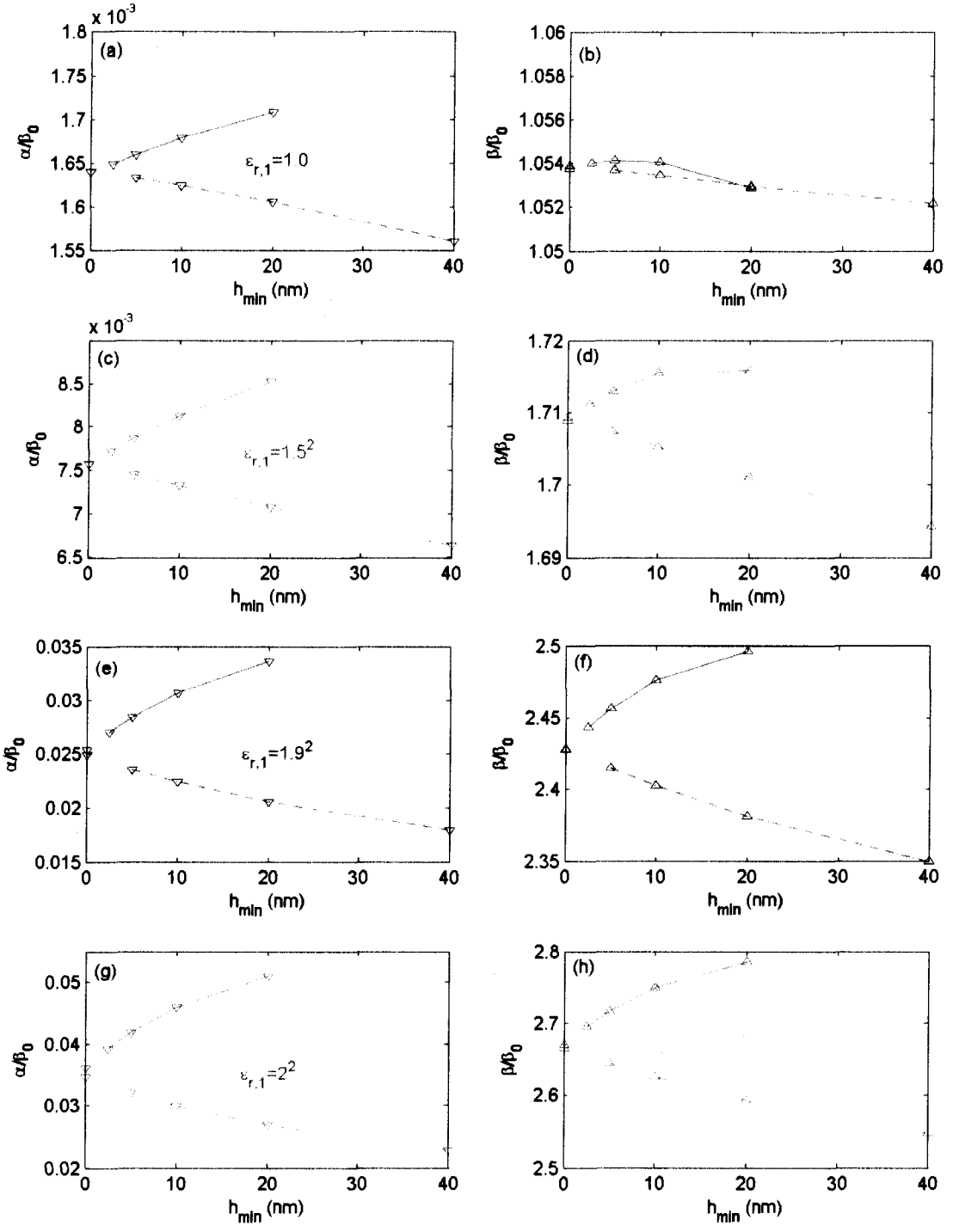

Fig. 10. Normalised attenuation and effective index of the mode supported by an isolated corner for λ_0 = 633 nm and $\varepsilon_{r,2}$ = -19-j0.53 as a function of discretisation for various values of $\varepsilon_{r,1}$. The computations were performed using the MoL (solid curves) and the FEM (dashed-dot curves). Extrapolated values are plotted at h_{min} = 0. (a) and (b) $\varepsilon_{r,1}$ = 1; (c) and (d) $\varepsilon_{r,1} = 1.5^2$; (e) and (f) $\varepsilon_{r,1} = 1.9^2$; (g) and (h) $\varepsilon_{r,1} = 2.0^2$.

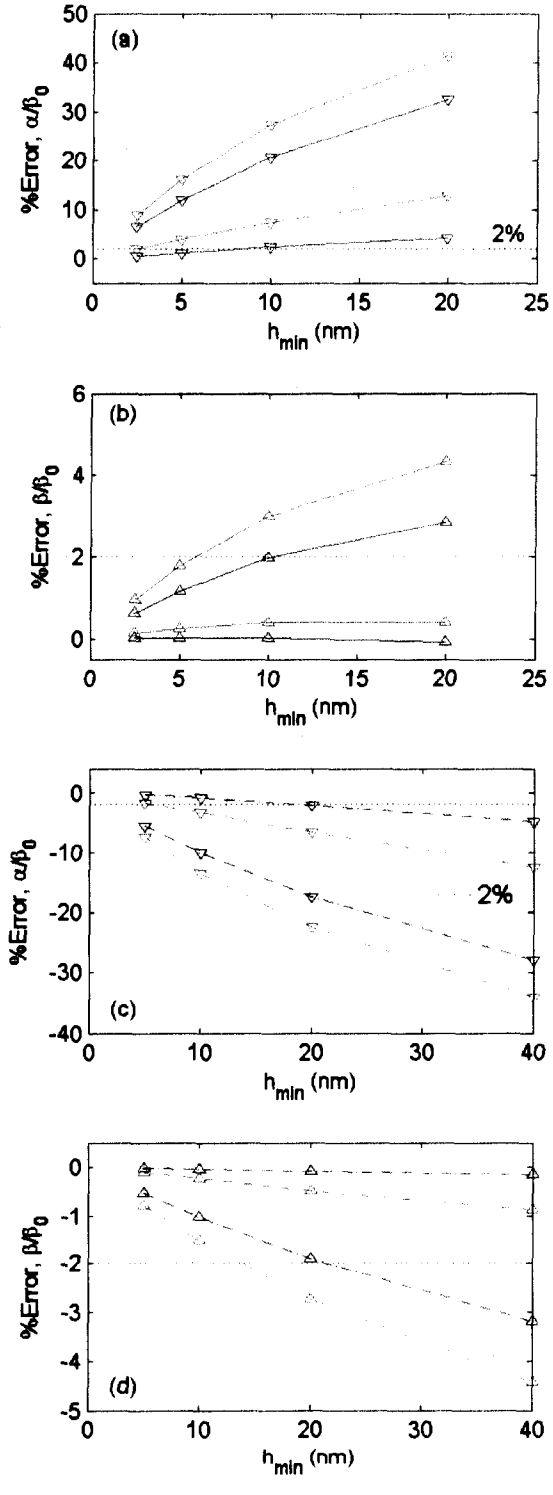

Fig. 11. Percentage errors in normalised attenuation ((a) and (c)) and in effective index ((b) and (d)) relative to the extrapolated values for the results given in Fig. 9 (plotted here using the same symbols, line styles and colours). The 2% error line is also plotted on each graph. The computations were performed using the MoL (solid curves, (a) and (b)) and the FEM (dashed-dot curves, (c) and (d)).

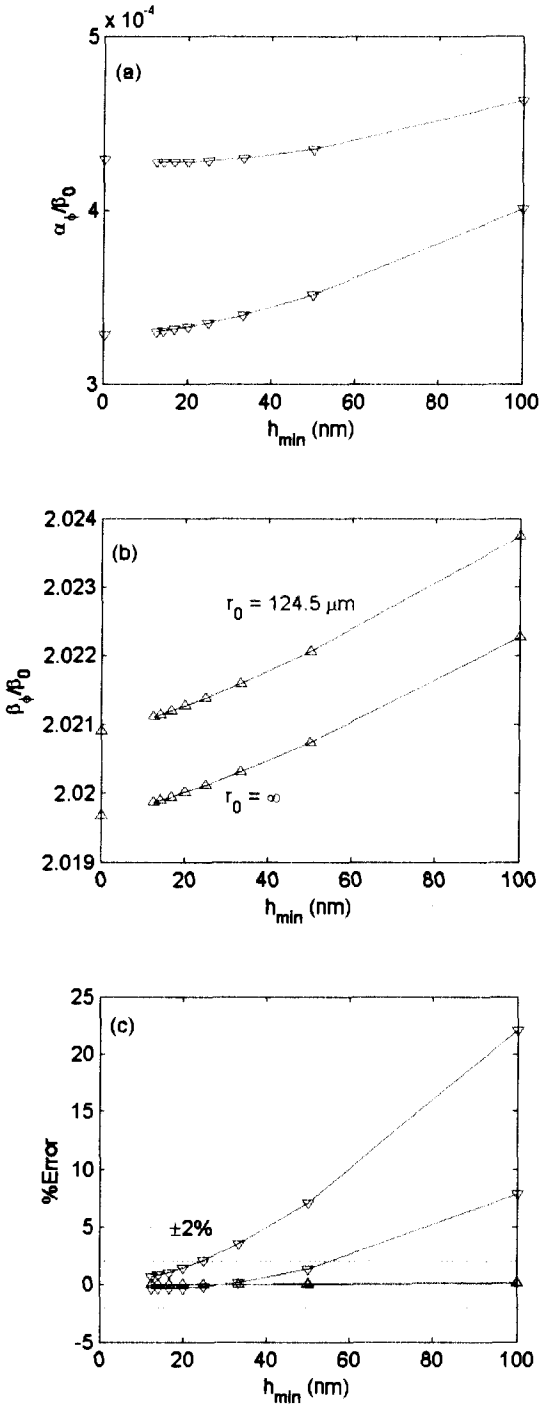

Fig. 12. (a) Normalised attenuation and (b) effective index of the ss_b^0 mode for w = 1 μm, t = 15 nm, λ_0 = 633 nm, $\varepsilon_{r,1}$ = 4 and $\varepsilon_{r,2}$ = -19-j0.53 as a function of discretisation, and for two radii of curvature ($r_0 = \infty$ and 124.5 μm). The computations were performed using the MoL for curves. Extrapolated values are plotted at $h_{min} = 0$. (c) Percentage errors relative to the extrapolated values; ±2% error lines are also plotted. The curves for the effective index overlap perfectly on this plot.

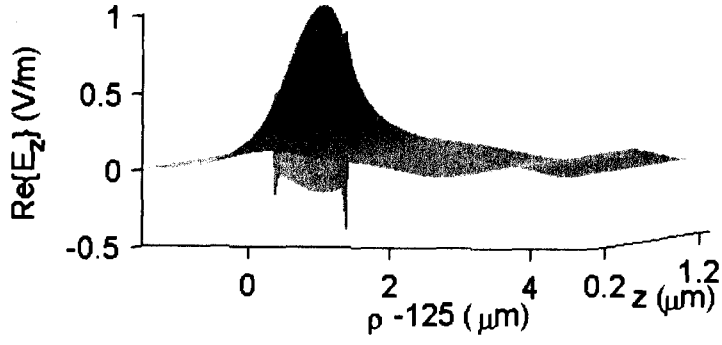

Fig. 13. Normalised Re$\{E_z\}$ of the ssb^0 mode for w = 1 μm, t = 15 nm, r_0 = 124.5 μm, λ_0 = 633 nm, $\varepsilon_{r,1}$ = 4 and $\varepsilon_{r,2}$ = -19-j0.53. Computations performed using the MoL for curves with $h_{min} \cong$ 50 nm.

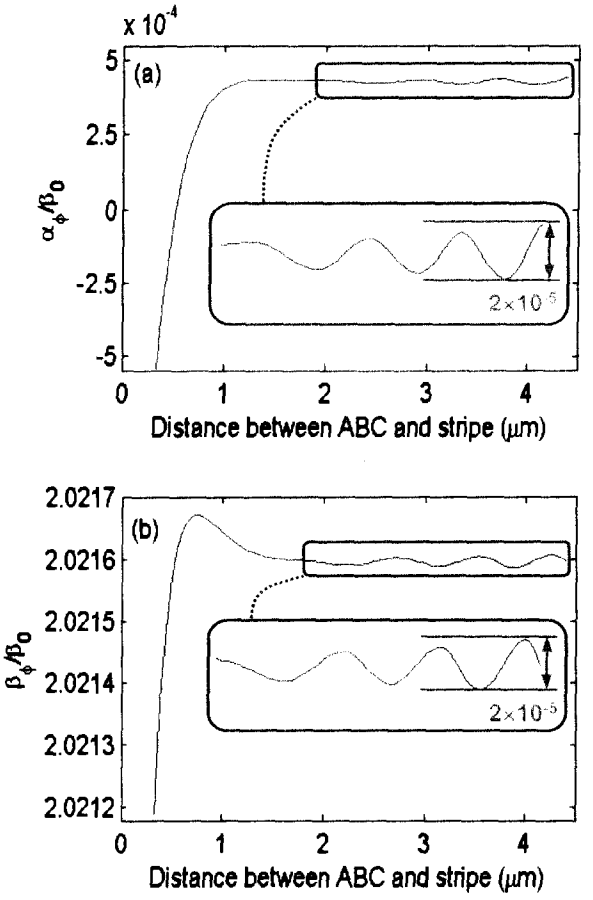

Fig. 14. (a) Normalised attenuation and (b) effective index of the $ss_b{}^0$ mode for w = 1 μm, t = 15 nm, r_0 = 124.5 μm, λ_0 = 633 nm, $\varepsilon_{r,1}$ = 4 and $\varepsilon_{r,2}$ = -19-j0.53 as a function of the distance between the right edge of the stripe and the absorbing boundary condition (ABC). The computations were performed using the MoL for curves with $h_{min} \cong 30$ nm.